The Far#Infrared Spectral Energy Distributions of X#Ray–selected Active Galaxies

Citation

Published Version

Permanent link

http://nrs.harvard.edu/urn-3:HUL.InstRepos:30238863

Terms of Use

Share Your Story

Accessibility

THE FAR-INFRARED SPECTRAL ENERGY DISTRIBUTIONS OF X-RAY–SELECTED ACTIVE GALAXIES[1]

Joanna K. Kuraszkiewicz and Belinda J. Wilkes
Harvard-Smithsonian Center for Astrophysics, 60 Garden Street, Cambridge, MA 02138;
jkuraszkiewicz@cfa.harvard.edu, bwilkes@cfa.harvard.edu

Eric J. Hooper
Department of Astronomy, University of Texas, Austin, TX 78712; ehooper@astro.as.utexas.edu

Kim K. McLeod
Astronomy Department, Wellesley College, Wellesley, MA 02481; kmcleod@wellesley.edu

Kenneth Wood
Department of Physics and Astronomy, University of St. Andrews, St. Andrews, Scotland; kw25@st-andrews.ac.uk

Jon Bjorkman
Ritter Observatory, Department of Physics and Astronomy, University of Toledo, Toledo, OH 43606; jon@astro.utoledo.edu

Kisha M. Delain
Department of Astronomy, University of Minnesota, Minneapolis, MN 55455; kdelain@astro.umn.edu

David H. Hughes
Instituto National de Astrofisica, Optica y Electronica, Mexico; dhughes@inaoep.mx

Martin S. Elvis
Harvard-Smithsonian Center for Astrophysics, 60 Garden Street, Cambridge, MA 02138; melvis@cfa.harvard.edu

Chris D. Impey
Steward Observatory, University of Arizona, Tucson, AZ 85721; impey@as.arizona.edu

Carol J. Lonsdale
IPAC, California Institute of Technology, 100-22, Pasadena, CA 91125; cjl@ipac.caltech.edu

Matt A. Malkan
Astronomy Department, University of California, Los Angeles, CA 90095; malkan@bonnie.astro.ucla.edu

Jonathan C. McDowell
Harvard-Smithsonian Center for Astrophysics, Cambridge, MA 02138; jmcdowell@cfa.harvard.edu

and

Barbara Whitney
Space Science Institute, Boulder, CO 80303; bwhitney@colorado.edu
Received 2002 October 23; accepted 2003 February 21

ABSTRACT

Hard X-ray selection is, arguably, the optimal method for defining a representative sample of active galactic nuclei (AGNs). Hard X-rays are unbiased by the effects of obscuration and reprocessing along the line of sight intrinsic/external to the AGN, which result in unknown fractions of the population being missed from traditional optical/soft X-ray samples. We present the far-infrared (far-IR) observations of 21 hard X-ray–selected AGNs from the *HEAO 1* A2 sample observed with *Infrared Space Observatory* (*ISO*). We characterize the far-IR continua of these X-ray–selected AGNs and compare them with those of various radio and optically selected AGN samples and with models for an AGN-heated, dusty disk. The X-ray–selected AGNs show broad, warm IR continua covering a wide temperature range ($\sim$20–1000 K in a thermal emission scenario). Where a far-IR turnover is clearly observed, the slopes are less than 2.5 in all but three cases so that nonthermal emission remains a possibility, although the presence of cooler dust resulting in a turnover at wavelengths longward of the *ISO* range is considered more likely. The sample also shows a wider range of optical/UV shapes than the optical/radio-selected samples, extending to redder near-IR colors. The bluer objects are type 1 Seyfert galaxies, while the redder AGNs are mostly intermediate or type 2 Seyfert galaxies. This is consistent with a modified unification model in which obscuration increases as we move from a face-on toward a more edge-on line of sight. However, this relation does not extend to the mid-infrared as the 25/60 μm ratios are similar in Seyfert galaxies with differing type and optical/UV reddening. The resulting limits on the column density of obscuring material through which we are viewing the redder AGNs ($N_{\rm H} \sim 10^{22}$ cm^{-2}) are inconsistent with standard optically thick torus models ($N_{\rm H} \sim 10^{24}$ cm^{-2}) and simple unification models. Instead our results support more complex models in which the amount of obscuring

material increases with viewing angle and may be clumpy. Such a scenario, already suggested by differing optical/near-IR spectroscopic and X-ray AGN classifications, allows for different amounts of obscuration of the continuum emission in different wave bands and of the broad emission line region, which, in turn, results in a mixture of behaviors for AGNs with similar optical emission-line classifications. The resulting decrease in the optical depth of the obscuring material also allows the AGN to heat more dust at larger radial distances. We show that an AGN-heated, flared, dusty disk with mass of $\sim 10^9 \, M_\odot$ and size of approximately a few hundred parsecs is able to generate optical–far-IR spectral energy distributions (SEDs) that reproduce the wide range of SEDs present in our sample with no need for an additional starburst component to generate the long-wavelength, cooler part of the IR continuum.

Subject headings: galaxies: active — galaxies: nuclei — infrared: galaxies — X-rays: galaxies

1. INTRODUCTION

Active galactic nuclei (AGNs) are among the broadest wave-band emission sources in nature, producing significant flux over a span more than 9 decades in frequency, from radio to X-rays and beyond (Elvis et al. 1994). The various emission mechanisms involved are presumably ultimately powered by a central supermassive black hole (Rees 1984).

A substantial fraction of the bolometric luminosity of many AGNs emerges in the infrared (IR), from synchrotron radiation and dust. Which of these is the principal emission mechanism is related to quasar type and is an open question in many cases (Wilkes 1999). Nonthermal emission is paramount in core-dominated radio-loud quasars and blazars (Impey & Neugebauer 1988), although hot dust contributes in some cases (Courvoisier 1998). The nonthermal component is likely related to radio and higher frequency synchrotron radiation (Chini, Kreysa, & Bierman 1987), providing information about the relativistic plasma and magnetic fields associated with quasars. Other AGN classes show evidence for a predominant dust contribution (Edelson & Malkan 1987), particularly infrared-luminous radio-quiet quasars (Hughes et al. 1993), or a mix of emission components (Haas et al. 1998). Much of the dust emission is due to heating by higher energy photons from the active nucleus and is therefore important for understanding the overall energy balance. The AGN thermal component may be an orientation-independent parameter, useful for examining unification hypotheses.

The nature of the foremost IR emission source is ambiguous in many AGNs with sparsely sampled spectral energy distributions (SEDs). Dust with smooth spatial and temperature distributions can mimic a power-law spectrum (Rees et al. 1969; Bollea & Cavaliere 1976), particularly in the absence of detailed measurements to reveal bumps from temperature and density inhomogeneities. Grain emissivity is characterized by a Planck function multiplied by a power-law factor $\propto \nu^1 - \nu^2$ (Hildebrand 1983), so spectral slopes in the Rayleigh-Jeans region of the coldest potential thermal component lie between $\alpha = 2$–4, depending on the grain properties and optical depth. Known synchrotron emitters have relatively flat submillimeter power-law spectra ($\alpha \leq 1.1$ and $f_\nu \propto \nu^\alpha$; Gear et al. 1994), and radio sources generally have spectra flatter than the canonical $\alpha = 2.5$ for a self-absorbed homogeneous synchrotron source (O'Dea 1998). Therefore, $\alpha = 2.5$ is a convenient partition to distinguish thermal emission from standard nonthermal models, and simple two-point spectral slopes and even lower limits to spectral indices may reveal the dominant mechanism (Chini et al. 1987). However, synchrotron models with a concave electron energy distribution (de Kool & Begelman

1989; Schlickeiser, Biermann, & Crusius-Wätzel 1991), free-free absorption, or plasma suppression (Schlickeiser & Crusius 1989) can produce slopes steeper than $\alpha = 2.5$. While $\alpha = 4$ is observed in some milliarcsecond radio knots (Matveyenko & Witzel 1999), thermal models offer the most consistent explanation for steep far-IR to millimeter slopes (Hughes et al. 1993; Andreani, Franceschini, & Granato 1999). A thermal origin is considered to be the most likely explanation for submillimeter/far-IR slopes $\alpha > 2.5$ in the present work.

The unified models of AGNs (e.g., Antonucci 1993) claim that the difference between the broad-line AGNs, such as Seyfert 1 galaxies, and narrow-line AGNs, such as Seyfert 2 galaxies, is due to orientation of a circumnuclear, dusty, torus-like structure. The dust absorbs the emission from the central nucleus and reradiates it in the IR. The first models of thermal IR emission in AGNs included simple models as in Barvainis (1987), where the optically thin (in IR) dust is distributed smoothly in a disklike configuration or as in Laor & Drain (1993), who considered a simple slab geometry. Sanders et al. (1989) proposed a warped, dusty disk extending into the host galaxy. Recent models of the absorbing structure around the active nucleus have invoked an axisymmetric, torus-like geometry, which is either compact ($r \leq$ few parsecs) with large optical thickness ($N_H \sim 10^{24}$ cm^{-2} and $\tau \sim 1000$ in the UV), as in Pier & Krolik (1992), or extended (tens to hundreds of parsecs in diameter) with moderate ($\tau = 10$–300 in UV) optical depth, as in Granato, Danese, & Franceschini (1997; see also: Granato & Danese 1994; Fadda et al. 1998; Efstathiou & Rowan-Robinson 1995). The extended models have been confirmed by the observation of large (~ 100 pc) extended dusty disklike structures around NGC 4261 (Jaffe et al. 1993) and NGC 1068 (e.g., Young et al. 1996), while the moderate optical depth was confirmed by the detection of broad near-IR emission lines in optically narrow-lined AGNs (Heisler & De Robertis 1999) and by the weakness of the 10 μm silicate absorption feature in Seyfert 1 galaxies (Roche et al. 1991).

Two large, complementary *Infrared Space Observatory* (*ISO*) AGN observing programs have opened up new wavelength windows in the far-IR as well as improving the spatial resolution and sampling at shorter wavelengths: the *ISO* European Central Quasar Program (Haas et al. 1998, 2000) and the NASA/*ISO* Key Project on AGNs, discussed herein. These observations directly measure the far-IR spectral slopes in low- and moderate-redshift AGNs and provide better constraints on the emission mechanisms throughout the IR region. Some of the fundamental questions being addressed with the new data include the range of SEDs within each AGN type, differences between one type and another and correlations with fluxes at other wave

bands, and orientation indicators. This paper focuses on a random subset of the hard X-ray–selected AGNs (Grossan 1992) in the *HEAO* catalog (Wood et al. 1984). The advantage of hard X-ray selection over selection in other wave bands is the lack of a strong bias against sources with significant line-of-sight absorption. Optical and soft X-ray samples, in particular, are strongly affected and may miss a large fraction of the AGN population as a whole (Masci, Drinkwater, & Webster 1999; Webster et al. 1995). The current sample thus provides an improved estimate of the range of SEDs present in the AGN population as a whole as well as an estimate of the fraction of the population missing from other surveys.

2. OBSERVATIONS AND DATA ANALYSIS

2.1. *The Sample: Hard X-Ray–selected AGNs*

Infrared and X-ray data complement each other well and are important for understanding the overall AGN energy balance. Nonthermal IR emission is possibly connected to the X-ray emission, either directly as part of a broad synchrotron component or as part of a radio-infrared seed spectrum that Compton scatters to produce the X-rays (see Wilkes 1999 for a review). Infrared data from dust-dominated sources reveal the level of ultraviolet (UV) and soft X-ray radiation that has been reprocessed and provide crude estimates of the temperature and mass of the dust.

Most X-ray–selected AGNs to date have been found in soft X-ray bands less than 3.5 keV (e.g., Stocke et al. 1991; Thomas et al. 1998; Beuermann et al. 1999; Schwope et al. 2000). Similar to optically selected samples, soft X-ray samples are biased against obscured sources, in this case because of absorption by the gas associated with the dust responsible for the optical obscuration. The absorption cross section drops steeply with increasing energy (Zombeck 1990), so that hard X-ray selection is much less affected by intervening material. Surveys in hard X-rays arguably are the most efficient way to distinguish between accreting and stellar sources (Fiore et al. 1999) as well as the optimal method for defining a representative sample of AGNs (Wilkes et al. 1999). A comparison between the absorbed UV/soft X-ray flux and the far-IR emission provides an estimate of the relative importance of accretion and stellar power in AGNs.

Hard X-ray samples (hereafter meaning those selected in the 2–10 keV band)[2] have been difficult to obtain and are limited in number of sources, depth, and redshift (although this is changing rapidly with the advent of *Chandra* and *XMM-Newton*) (Hornschemeier et al. 2001; Brandt et al. 2001; Barger et al. 2001; Tozzi et al. 2001; Wilkes et al. 2001; Hasinger et al. 2001). One of the best-studied samples is that of Piccinotti et al. (1982), derived from a large-area 2–10 keV survey using the A2 experiment onboard the *HEAO 1* satellite (Giacconi et al. 1979; Marshall et al. 1979; Boldt 1987). This sample contains 35 $z \leq 0.17$ AGNs, mostly Seyfert 1 galaxies (Kotilainen et al. 1992; Malizia et al. 1999). Improvements in analysis techniques pushed the flux limits deeper (Jahoda & Mushotzky 1989), with a corresponding increase in the number of cataloged sources. We randomly selected 21 targets from an expanded compilation of *HEAO 1* A2 AGNs (Grossan 1992), 12 of which are also in the Piccinotti sample.

---

[2] Because of this definition, Mrk 478, which has a very steep soft X-ray spectrum, is included in our sample as being sufficiently bright in the 2–10 keV band.

TABLE 1
SAMPLE

Name	z	Seyfert Type	α (J2000.0)	δ (J2000.0)
Mrk 1152	0.053	1.5	01 13 50.09	−14 50 46.5
Mrk 590	0.026	1.2	02 14 33.56	−00 45 59.9
ESO 198−G24	0.046	1	02 38 19.52	−52 11 31.5
3A 0557−383	0.034	1	05 58 02.92	−38 20 05.7
PG 0804+761.............	0.100	1	08 10 56.31	+76 02 43.0
H1039−074...............	0.674	...	10 42 19.16	−07 40 35.4
NGC 3783..................	0.010	1	11 39 01.77	−37 44 19.7
Ton 1542....................	0.063	1	12 32 03.60	+20 09 30.0
IRAS 13218+0552......	0.205	1	13 24 21.58	+05 36 57.1
MCG −6-30-15...........	0.008	1.2	13 35 53.93	−34 17 42.5
IC 4329A	0.016	1.2	13 49 19.39	−30 18 35.3
H1419+480.................	0.072	1	14 21 29.42	+47 47 27.8
Mrk 478	0.079	1	14 42 07.47	+35 26 23.0
H1537+339.................	0.330	1	15 39 52.23	+33 49 31.1
KAZ 102	0.136	1	18 03 28.80	+67 38 10.0
E1821+643	0.297	1	18 21 54.89	+64 21 12.1
H1834−653.................	0.013	2	18 38 20.28	−65 25 41.8
Mrk 509	0.034	1.2	20 44 09.74	−10 43 24.5
NGC 7213..................	0.006	1.5	22 09 16.58	−47 09 36.0
MR 2251−178	0.064	1	22 54 05.10	−17 34 47.0
MCG −2-58-22...........	0.047	1.5	23 04 43.48	−08 41 08.7

NOTE.—Units of right ascension are hours, minutes, and seconds, and units of declination are degrees, arcminutes, and arcseconds.

We confirmed that our subset is representative of the whole sample of *HEAO* AGNs by comparing their optical and near-IR colors, concluding that they have a greater than an 80% chance of coming from the same population as the full sample (Kolmogorov-Smirnov [K-S] test). In this paper we analyze these *HEAO* targets. Their redshift, coordinates, and Seyfert type were taken from the NASA Extragalactic Database (NED)[3] and are presented in Table 1.

2.2. *ISO Observations and Data Reduction*

The Key Project sample consists of 5–200 μm chopped and rastered ISOPHOT (Lemke et al. 1996) observations of 73 AGNs selected to incorporate a wide range of AGN types and redshifts. Eight broadband ISOPHOT filters were employed: 4.85, 7.3, 11.5, 25, 60, 100, 135, and 200 μm. Most of the sources (53 of 72) were observed in a rectangular chop mode, the point-source detection technique preferred at the beginning of the *ISO* mission. Concerns about calibrating and interpreting chopped measurements, particularly at long wavelengths, led to a switch to small raster scans. We reobserved 18 of the chopped fields and switched 19 additional targets from our original list to raster mode. The change in observing strategy, combined with lower than expected instrumental sensitivity, resulted in a halving of the originally planned sample. However, data from both observing modes are now available for a subset of the targets, providing a crosscheck and better information about background variations from the raster maps.

The data are reduced using a combination of the (ISO-)PHOT Interactive Analysis (PIA; Gabriel, Acosta-Pulido, & Heinrichsen 1998) software plus custom scripts (Hooper

---

[3] The NASA/IPAC Extragalactic Database (NED) is operated by the Jet Propulsion Laboratory, California Institute of Technology, under contract with the National Aeronautics and Space Administration.

et al. 1999). Raster maps have proven to be relatively reliable and are now considered scientifically validated. Short wavelength ($\lambda \leq 25 \mu$m) chopped data obtained with the P1 and P2 detectors are also fairly robust, but chopped measurements using the long-wavelength C1 and C2 arrays are still somewhat problematic (see the comparison with *IRAS* fluxes in Hooper et al. (1999). Some of the difficulty lies with vignetting corrections, particularly for the C2 detector, in which the source is centered at the convergence of 4 pixels (Hooper et al. 1999). Detector drift may impart to the vignetting correction an apparent dependence on chopper dwell time and brightness (M. Haas 2003, private communication), an effect that is currently being investigated.

The *ISO* fluxes for subset of the *HEAO 1* A2 sample are presented in Table 2.

2.3. *Spectral Energy Distributions*

The *ISO* points described above were combined with literature data spanning from radio to hard X-ray (see Table 3 for details) and complemented with our own near-IR photometry to generate the most comprehensive SEDs possible. We derived near-IR (JHK_s) photometry from images obtained on the Steward Observatory 61 inch telescope on Mount Bigelow during the period 1995 June–1996 March. We used a 256×256 NICMOS array camera with the pixel scale set to $0\farcs9$. To maximize on-source integration time and to ensure proper monitoring of the sky, we took the images in a 4×4 raster pattern for each filter. Typical times at each raster position varied from 1 to 60 s, chosen to avoid saturating the detector. The 16 frames in each raster were used along with a dark frame of the same exposure time to construct median sky frames and normalized flats. A clipping algorithm used during median filtering ensured that the wings of the point sources were eliminated. The reduced images were aligned and averaged to produce a final image for each raster. Elias photometric standard stars (Elias et al. 1982) observed in the same manner provided aperture fluxes accurate to 5%–10% on nights with usable data. The *JHK* photometry is presented in Table 4. In Mrk 1152 we include in the SED the optical spectrophotometry carried out on 1996 October 7, with the FAST spectrograph on the 1.5 m Tillinghast Telescope on Mount Hopkins in Arizona, using an ~3 inch aperture. To provide flux calibration, a standard star was observed through the same aperture, at similar air mass, immediately after the AGN observation. We reduced the data in a standard manner using IRAF[4] (see Tokarz & Roll 1997 for details) and then fitted a continuum to the spectrum (using IRAF task *continuum*), which was next binned into broader wavelength bands and included in the SED.

For comparison with the *ISO* data we also included observations from the *Infrared Astronomical Satellite* (*IRAS*). In one object (PG 0804+761), however, the *ISO* chopped flux at 100 μm differed from the flux obtained with *IRAS*. We decided to discard the *ISO* 100 μm flux in this object, as the C2 detector measurements in chopped mode may not be reliable (see previous section), and included only the *IRAS* flux. In a number of objects (Ton 1542, MCG −6-30-15, IC 4329A, H1419+480, E1821+643, Mrk 509,

and MR 2251−178) we also decided to omit the chopped 12 μm *ISO* flux, as it differed considerably from the *IRAS* flux and did not follow the overall SED shape.

A correction for Galactic extinction was applied to each SED, which was determined using the reddening values obtained from the literature (see Table 3 for details). After correction for Galactic extinction, the data were blueshifted to the rest frame using a cosmological model with $q_0 = 0$ and $H_0 = 50$ km s^{-1} Mpc^{-1}. No *K*-correction was applied since we were working with complete SEDs. The contribution from the host galaxy was subtracted using the method and template of Elvis et al. (1994; based on the Sbc galaxy model of Coleman, Wu, & Weedman 1980) and normalized by the host galaxy monochromatic luminosity in the *H* band (or *V* band when *H* was not available) obtained from the literature (see Table 3 for details). If an AGN had more than one data point in a single frequency bin, we calculated an average [in $\log \nu f(\nu)$] of those observation points and included one data point in the SED. The final SEDs are displayed in Figure 1 in order of right ascension.

In order to better characterize the SEDs, we directly measured various IR luminosities and slopes (presented in Table 5) as well as the optical, UV, X-ray, and bolometric luminosities (presented in Table 6). The SEDs were linearly interpolated between the observational points, while the EUV continuum was determined by interpolating between the highest energy UV data point and the lowest energy soft X-ray point estimated from the observed flux and spectral slope α_x ($f_\nu \propto \nu^{\alpha_x}$). If the soft X-ray spectral slope was unknown the slope $\alpha_x = -1$ was assumed.

We also plot a median AGN energy distribution in the *UVOIR* range normalized to 1.5 μm in Figure 2 with the 68, 90, and 100 Kaplan-Meier percentile envelopes (see Feigelson & Nelson 1985; Isobe, Feigelson, & Nelson 1986) to allow comparison with other samples. The median SED shows a large dispersion from the mean both in the IR and optical/UV.

3. THE INFRARED SPECTRAL ENERGY DISTRIBUTIONS

3.1. *Characteristics*

A closer look at the SEDs of the *HEAO* sample (Fig. 1) reveals that 13 of 21 objects show either a minimum at 1 μm (if the big blue bump is present) or a downturn at 1 μm from the mid-IR (if the big blue bump is highly reddened), consistent with a drop in opacity at the dust sublimation temperature ~2000 K (Sanders et al. 1989). The remainder show either no minimum/downturn (five objects) or do not have enough data points around 1 μm to detect the dip (three objects). Three of five objects with no minimum/downturn at 1 μm, show steep ($\geq$2.5) far-IR cutoff slopes (MR 2251−178 has $\alpha_{cut} = 3.7$, while MCG −2-58-22 and E1821+643 have $\alpha_{cut} = 2.5$) that indicate thermal dust emission (see § 1; far-IR cutoff slopes are presented in Table 7). The remining 18 AGNs have slopes flatter than $\alpha_{cut} = 2.5$, which can be interpreted either as dust emission in which the lowest temperature dust emits at wavelengths longer than our coverage (i.e., $\lesssim$40 K) or as inhomogeneous, nonthermal synchrotron emission. While we cannot rule out nonthermal emission, we assume that the IR is dominated by dust emission in our ensuing discussion.

---

[4] IRAF (Image Reduction and Analysis Facility) is distributed by the National Optical Astronomy Observatory, which are operated by AURA, Inc., under cooperative agreement with the National Science Foundation.

TABLE 2
ISO FLUXES

Name	5 μm	7 μm	12 μm	25 μm	C or R[a]	60 μm	100 μm	C or R[a]	135 μm	200 μm	C or R
Mrk 1152	...	...	...	...	...	0.213 ± 0.022	0.445 ± 0.017	R	0.547 ± 0.030	0.321 ± 0.041	R
Mrk 590	0.019 ± 0.003	0.322 ± 0.003	0.288 ± 0.005	0.390 ± 0.013	R	0.432 ± 0.020	1.135 ± 0.036	R	1.802 ± 0.053	1.609 ± 0.064	R
ESO 198−G24	...	0.058 ± 0.003	0.071 ± 0.005	0.082 ± 0.013	R	0.107 ± 0.020	0.128 ± 0.023	R	0.051 ± 0.031	0.009 ± 0.040	R
3A 0557−383	0.011 ± 0.003	0.220 ± 0.003	0.348 ± 0.005	0.505 ± 0.013	R	0.221 ± 0.036	0.151 ± 0.046	R	0.172 ± 0.014	0.117 ± 0.040	R
PG 0804+761	0.020 ± 0.003	0.217 ± 0.003	0.195 ± 0.005	0.246 ± 0.013	R	0.145 ± 0.020	0.097 ± 0.024	R	0.072 ± 0.018	0.051 ± 0.040	R
H1039−074	<0.006	0.014 ± 0.003	0.086 ± 0.020	0.053 ± 0.019	C	<0.060	<0.090	C	<0.150	<0.210	C
NGC 3783	...	0.487 ± 0.015	1.976 ± 0.031	2.934 ± 0.097	C	...	...	...	3.910 ± 0.071	1.949 ± 0.182	C
Ton 1542	0.021 ± 0.003	0.045 ± 0.010	0.170 ± 0.096	0.190 ± 0.089	C	...	...	...	0.111 ± 0.036	0.105 ± 0.051	C
IRAS 13218+0552	0.100 ± 0.015	0.189 ± 0.014	0.338 ± 0.076	0.313 ± 0.015	C	3.01 ± 1.2	0.53 ± 0.21	C	0.270 ± 0.041	<0.180	C
MCG −6-30-15	0.126 ± 0.027	0.238 ± 0.015	0.687 ± 0.013	0.843 ± 0.319	C	...	...	...	0.584 ± 0.060	0.096 ± 0.100	C
IC 4329A	...	1.221 ± 0.020	3.089 ± 0.321	2.151 ± 0.077	C	...	1.384 ± 0.025	R	1.161 ± 0.040	0.763 ± 0.047	R
H1419+480	0.018 ± 0.012	0.099 ± 0.015	0.276 ± 0.029	0.260 ± 0.175	C	<0.603	<0.589	C	0.124 ± 0.051	<0.210	C
Mrk 478	0.037 ± 0.003	0.061 ± 0.005	0.121 ± 0.033	0.218 ± 0.049	C	...	...	C	0.457 ± 0.046	<0.600	C
H1537+339	0.004 ± 0.003	0.006 ± 0.003	...	0.070 ± 0.019	C	<0.150	<0.120	C	0.178 ± 0.031	0.170 ± 0.060	C
KAZ 102	0.038 ± 0.010	0.025 ± 0.015	...	...	R	<0.075	0.038 ± 0.010	R	0.152 ± 0.061	0.166 ± 0.085	C
E1821+643	...	0.195 ± 0.013	0.700 ± 0.107	0.745 ± 0.460	C	...	...	...	...	...	...
H1834−653	...	...	...	...	...	...	...	...	0.600 ± 0.051	0.306 ± 0.037	R
Mrk 509	0.128 ± 0.008	0.334 ± 0.003	0.847 ± 0.102	0.586 ± 0.164	C	...	...	C	...	0.225 ± 0.147	C
NGC 7213	...	...	...	...	...	...	3.67 ± 0.142	R	6.772 ± 0.340	5.463 ± 0.392	R
MR 2251−178	0.092 ± 0.005	0.133 ± 0.005	0.300 ± 0.070	0.152 ± 0.015	C	...	...	...	0.508 ± 0.042	0.225 ± 0.061	C
MCG −2-58-22	0.112 ± 0.021	0.176 ± 0.007	0.392 ± 0.220	0.238 ± 0.029	C	...	...	C	0.332 ± 0.050	0.154 ± 0.066	C

NOTE.—Fluxes are in Jy.

[a] C = chopped data, R = raster scans, for preceding columns of data.

132

TABLE 3

Spectral Energy Distributions Details for *HEAO* Sample

| Name (1) | References | | | | | | Starlight[a] (8) | Half-light Radius (9) | Reference[b] (10) | Galaxy N_H[c] (11) | Intrinsic Absorption?[d] (12) |
	Radio (2)	Submillimeter (3)	Far-IR (4)	Optical/Near-IR (5)	UV (6)	X (7)					
Mrk 1152	...	...	9, 30	9, 15, 25, 31	...	17, 22	43.87	...	34	1.67	No
Mrk 590	...	...	25, 30	14, 25	23	2, 22, 23	44.10	...	36, 37	2.60	No
ESO 198−G24	...	...	9, 30	25	24	24	43.26	...	34	5.41	No
3A 0557−383	...	...	9, 30	25	...	17, 20, 22	$44.60^{+0.30}_{-0.60}$	10.0	34	3.38	70^{+90}_{-40}
PG 0804+761	13	...	9, 21, 30	16, 7	7	7, 27	$44.38^{+0.12}_{-0.12}$	7.5	36	3.09	No
H1039−074	...	...	9, 30	9	...	28	$44.60^{+0.30}_{-0.60}$	10.0	...	3.75	?
NGC 3783	...	...	9, 30	9, 19	...	17, 22	43.50	...	34	9.01	No
Ton 1542	13	...	9, 21, 30	6, 9, 16	7	2, 4	$44.41^{+0.12}_{-0.12}$	7.5	32, 36	2.58	No
IRAS 13218+0552 ...	...	...	9, 5, 30	5, 9	...	18	$44.60^{+0.05}_{-0.60}$	10.0	...	2.30	?
MCG −6-30-15	...	...	9, 25, 30	9	23	17, 23	43.00	...	34	4.06	No
IC 4329A	...	...	9, 30	9, 19, 25	...	17, 22	42.62	...	34	4.55	15.0^{+4}_{-3}
H1419+480	...	...	9, 30	9	...	2, 18	$44.60^{+0.10}_{-0.60}$	10.0	...	1.72	No
Mrk 478	13	3	9, 30	9, 16, 19	8, 23	1, 2, 23	$44.31^{+0.12}_{-0.12}$	6.25	36	1.01	No
H1537+339	...	...	9, 30	18	...	18, 29	$44.60^{+0.30}_{-0.60}$	10.0	...	1.97	No
KAZ 102	11	...	9, 30	7, 9	7	2, 26	$43.86^{+0.04}_{-0.04}$	11.9	32	4.44	No
E1821+643	...	3, 10	9, 30	9	...	2, 27	$44.60^{+0.30}_{-0.60}$	10.0	33	3.50	No
H1834−653	...	3, 10	9, 25, 30	19, 15, 25	7	2, 17, 22	43.44	...	34	6.31	1350^{+330}_{-230}
Mrk 509	...	...	9, 30	9	...	17, 22	44.02	...	35	3.93	No
NGC 7213	...	...	9, 30	9	...	17, 22	43.64	...	34	3.00	No
MR 2251−178	11	...	9, 30	12, 14, 15	7	7, 22	$44.65^{+0.04}_{-0.04}$	12.2	32	2.82	No
MCG −2-58-22	...	...	30	14, 15, 25	23	17, 22, 23	$44.60^{+0.30}_{-0.60}$	10.0	34	3.47	No

[a] Log of host galaxy luminosity in *H* band, where half-light radius is quoted, otherwise log of luminosity in *V* band.

[b] References for cols. (8) and (9).

[c] Galactic column in units of 10^{20} cm^{-2}.

[d] Intrinsic N_H is in units of 10^{20} cm^{-2} from X-ray analysis; for references see col. (7).

References.—(1) Boller, Brandt, & Fink 1996; (2) Ceballos & Barcons 1996; (3) Chini et al. 1989; (4) Comastri et al. 1992; (5) Low et al. 1989; (6) Cutri et al. 1985; (7) Elvis et al. 1994; (8) Gondhalekar et al. 1994; (9) Grossan 1992; (10) Hughes et al. 1993; (11) Hutchings & Gower 1985; (12) Hutchings & Gower 1985; (13) Kellerman et al. 1989; (14) McAlary et al. 1983; (15) *HJK* photometry; this paper; (16) Neugebauer et al. 1987; (17) Piccinoti et al. 1982; (18) Remillard et al. 1993; (19) Rieke 1978; (20) Rush et al. 1996; (21) Sanders et al. 1989; (22) Turner & Pounds 1989; (23) Walter & Fink 1993; (24) Wang, Lu, & Zhou 1998; (25) Ward et al. 1987; (26) Wilkes & Elvis 1987; (27) Williams et al. 1992; (28) Wood et al. 1994; (29) Yuan et al. 1998; (30) *ISO* observations; this paper; (31) MMT optical spectra; this paper; (32) Hutchings, Crampton, & Campbell 1984; (33) Hutchings, Janson, & Neff 1989; (34) Kotilainen, Ward, & Williger 1993; (35) MacKenty 1990; (36) McLeod & Rieke 1994; (37) McLeod & Rieke 1995.
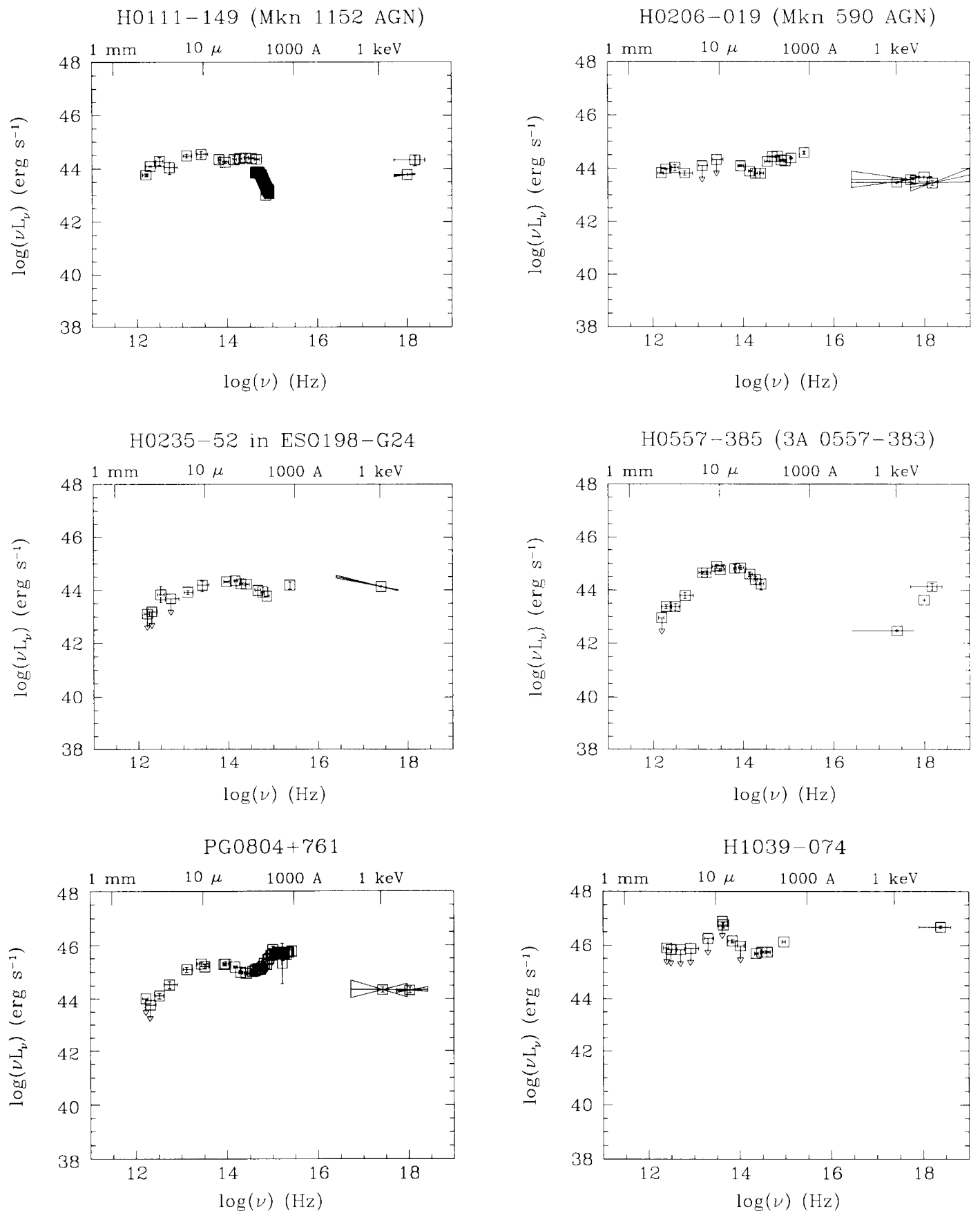
133

H0111−149 (Mkn 1152 AGN)

H0206−019 (Mkn 590 AGN)

H0235−52 in ESO198−G24

H0557−385 (3A 0557−383)

PG0804+761

H1039−074

Fig. 1.—Radio–to–X-ray SEDs for AGNs in our sample on a log νL_ν vs. log ν scale

H1136−375 in NGC 3783

TON 1542 (PG 1229+204)
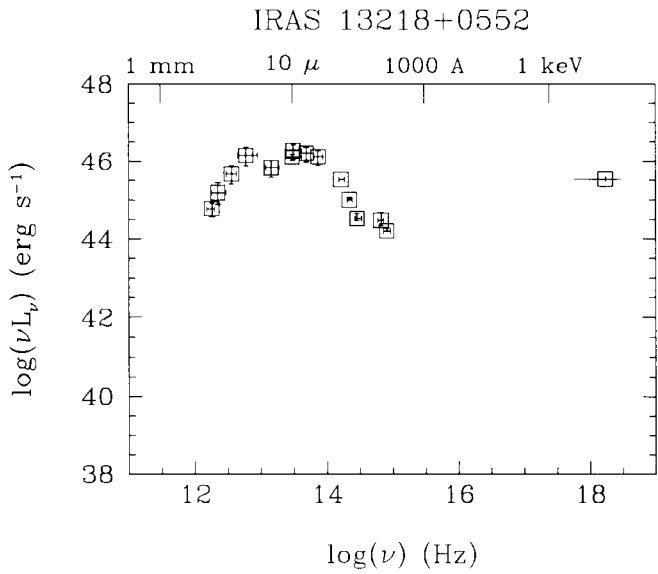

IRAS 13218+0552

H1332−336 in MCG −6−30−15

H1346−300 in IC 4329A

H1419+480

FIG. 1.—*Continued*

PG 1440+356 (Mkn 478 AGN)

H1537+339

Q1803+676 in Kazaryan 102

E1821+643

H1834−653 in ESO103−G35

H2041−109 (Mkn 509)

Fig. 1.—*Continued*
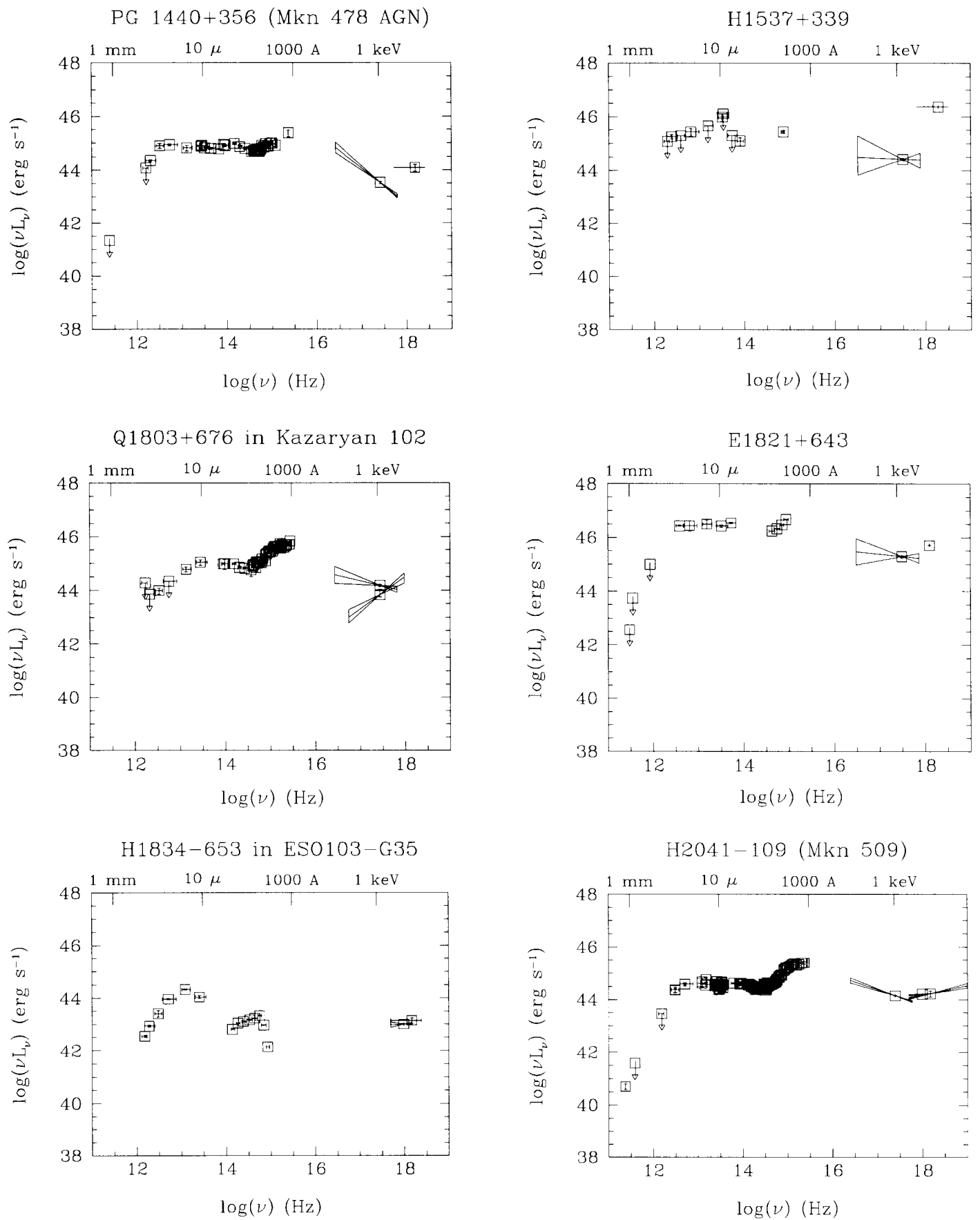
H2209−471 in NGC 7213
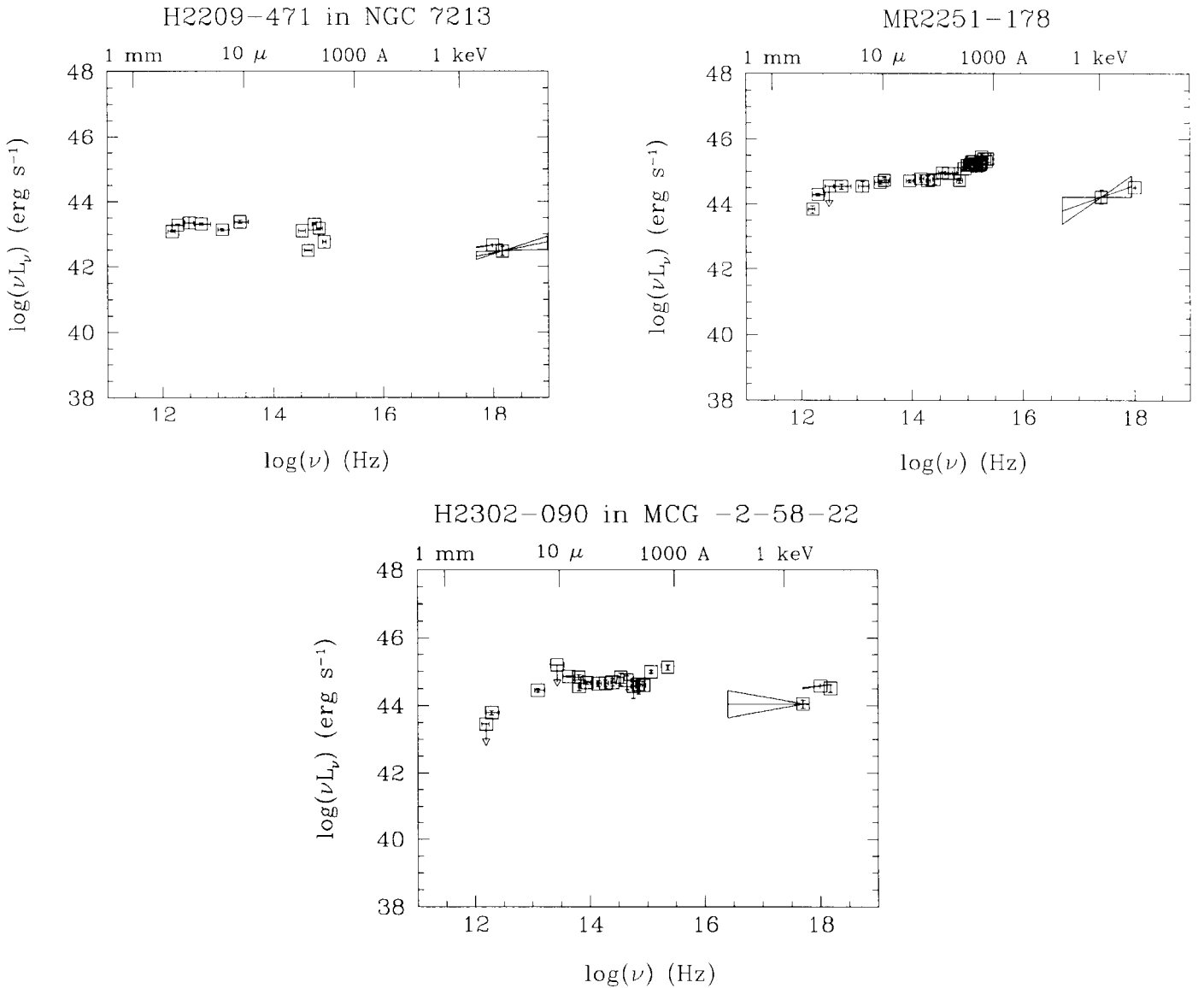

MR2251−178

H2302−090 in MCG −2−58−22
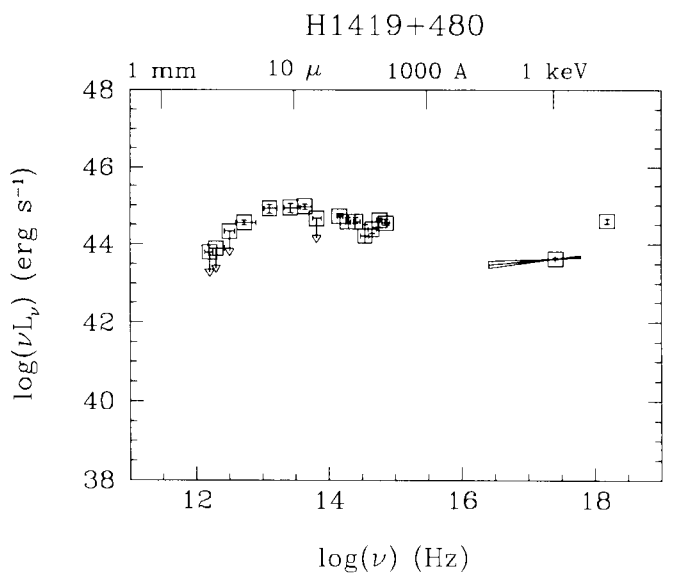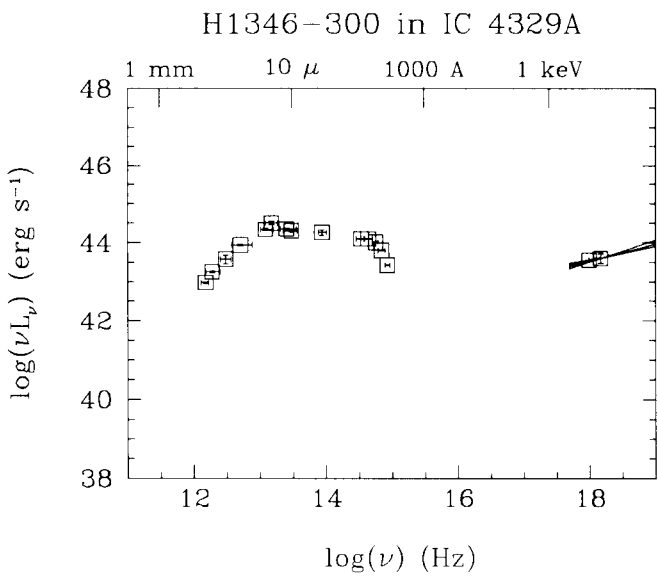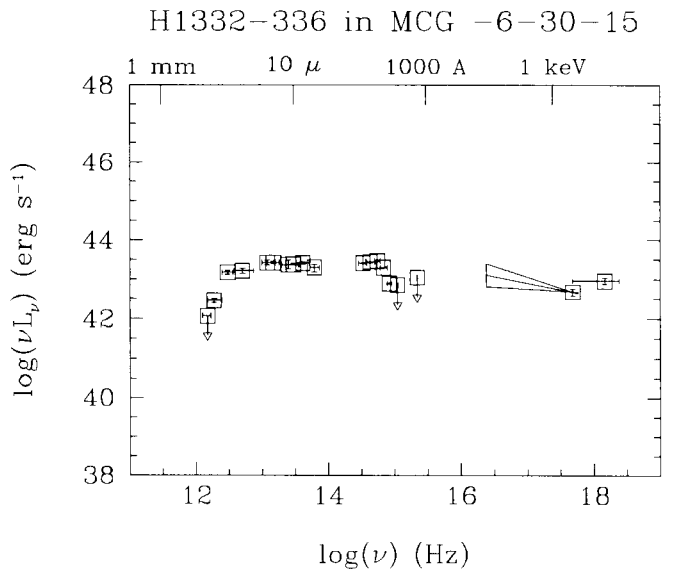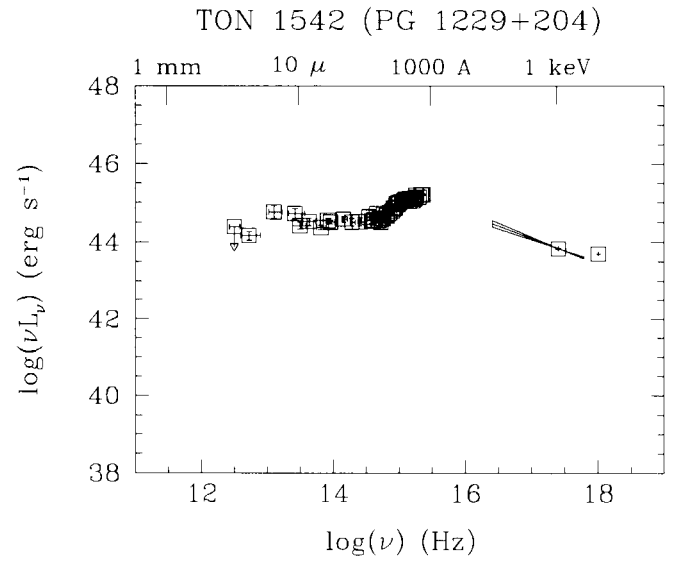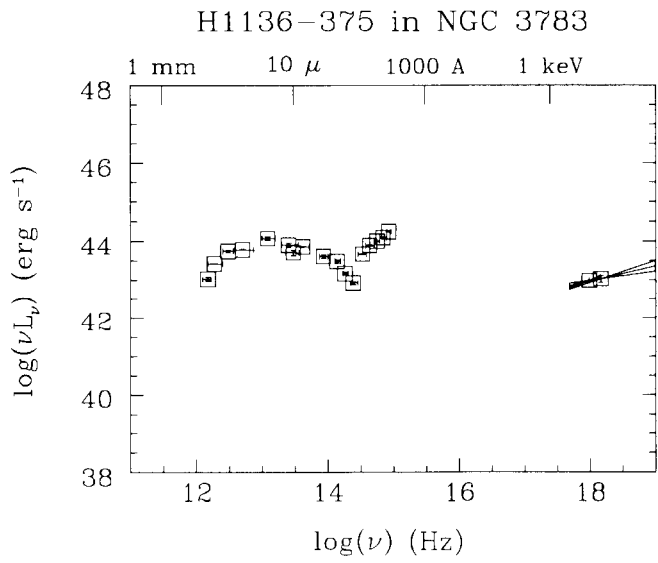
Fig. 1.—*Continued*

The IR SEDs cover a broad wavelength range indicating a wide range of temperatures in a thermal emission scenario. In Table 7 we list the maximum and minimum temperature of dust required to match the continuum observed, estimated for each object by comparing the observed data to graybody curves at various temperatures. An example is shown in Figure 3. The lowest indicated temperature is an upper limit when no long-wavelength turnover is observed in the *ISO* band. The number of data points is generally too few for formal fits to provide any useful constraints on the

dust temperature, but these rough values, which are similar to those reported in earlier studies, are too broad to be explained by optically thick dusty torus models and are generally attributed to a combination of AGN-heated torus emission and cooler emission from starburst-heated dust (Rowan-Robinson 1995).

3.2. *Comparison with Samples Selected in Other Wavebands*

As discussed above, X-ray selection is expected to find a somewhat different subset of the AGN population with less bias against sources that include intrinsic line-of-sight absorption. In this section we compare the SEDs of the *HEAO* sample with those of samples selected at optical, near-IR, and radio wavelengths in order to quantify this difference and understand the subset of the population that may have been missed from those samples.

We first compare the SEDs of our hard X-ray–selected AGN sample with those presented by Elvis et al. (1994, hereafter E94). The E94 sample consists of bright soft X-ray objects observed by the *Einstein Observatory* satellite, with

TABLE 4
NEAR-IR PHOTOMETRY

Name	J	H	K
Mrk 1152	12.63	11.90	11.37
Mrk 509	11.73	10.94	10.09
MR 2251−178	12.56	11.89	11.11
MCG −2-58-22..............	12.27	11.56	10.94

TABLE 5
IR LUMINOSITIES

Name	$L(1.6–3.2)$	$L(3.2–6.4)$	$L(6.4–12.8)$	$L(12.8–25)$	$L(25–50)$	$L(50–100)$	$L(1–10)$	$L(10–100)$	$L(3–60)$	$L(60–200)$	$L(1–200)$	$\log[F(25)/F(60)]$	$\alpha(25/60)$
Mrk 1152	$44.17^{+0.11}_{-0.11}$	$44.17^{+0.09}_{-0.11}$	$44.33^{+0.10}_{-0.13}$	$44.33^{+0.08}_{-0.10}$	$44.13^{+0.12}_{-0.15}$	$44.00^{+0.17}_{-0.19}$	$44.73^{+0.11}_{-0.13}$	$44.72^{+0.11}_{-0.13}$	$44.87^{+0.10}_{-0.12}$	$44.20^{+0.12}_{-0.12}$	$45.06^{+0.11}_{-0.12}$	−0.01	−0.03
Mrk 590	$43.69^{+0.02}_{-0.03}$	$43.88^{+0.11}_{-0.11}$	<44.12	<44.02	<43.86	$43.75^{+0.15}_{-0.20}$	$44.29^{+0.12}_{-0.41}$	$44.27^{+0.20}_{-0.17}$	$44.43^{+0.12}_{-1.28}$	$44.02^{+0.06}_{-0.07}$	$44.67^{+0.14}_{-0.40}$	−0.12	−0.32
ESO 198–G24	$44.16^{+0.02}_{-0.03}$	$44.13^{+0.06}_{-1.06}$	$44.06^{+0.13}_{-0.20}$	$43.87^{+0.11}_{-0.18}$	<43.70	<43.75	$44.63^{+0.05}_{-0.11}$	$44.29^{+0.17}_{-0.12}$	$44.59^{+0.08}_{-0.09}$	$43.43^{+0.42}$	$44.80^{+0.05}_{-0.09}$	−0.20	−0.53
3A 0557–383	$44.48^{+0.09}_{-0.09}$	$44.65^{+0.12}_{-0.07}$	$44.64^{+0.08}_{-0.07}$	$44.54^{+0.06}_{-0.18}$	$44.17^{+0.07}_{-0.06}$	$43.51^{+0.11}_{-0.13}$	$45.04^{+0.11}_{-0.44}$	$44.85^{+0.06}_{-0.44}$	$45.16^{+0.09}_{-0.09}$	$43.47^{+0.15}_{-0.19}$	$45.26^{+0.09}_{-0.09}$	0.44	1.16
PG 0804+761	$45.06^{+0.06}_{-0.06}$	$45.11^{+0.05}_{-0.05}$	$45.09^{+0.07}_{-0.07}$	$45.00^{+0.08}_{-0.09}$	$44.68^{+0.10}_{-0.12}$	$44.20^{+0.11}_{-0.17}$	$45.56^{+0.06}_{-0.06}$	$45.32^{+0.08}_{-0.10}$	$45.62^{+0.07}_{-0.08}$	$44.14^{+0.11}_{-0.36}$	$45.76^{+0.07}_{-0.07}$	0.22	0.58
H1039–074	$45.73^{+0.01}_{-0.01}$	$46.15^{+0.07}_{-0.07}$	$46.59^{+0.06}_{-1.14}$	<46.02	<45.75	<45.68	$46.67^{+0.03}_{-0.33}$	<46.46	$47.15^{+0.15}_{-0.97}$	⋯	$46.41^{+0.50}_{-0.50}$	−0.16	−0.42
NGC 3783	$43.29^{+0.04}_{-0.04}$	$43.55^{+0.03}_{-0.03}$	$43.66^{+0.04}_{-0.04}$	$43.83^{+0.05}_{-0.05}$	$43.80^{+0.03}_{-0.03}$	$43.61^{+0.02}_{-0.02}$	$43.95^{+0.03}_{-0.03}$	$44.28^{+0.04}_{-0.04}$	$44.35^{+0.04}_{-0.04}$	$43.71^{+0.02}_{-0.02}$	$44.48^{+0.03}_{-0.03}$	−0.13	−0.34
Ton 1542	$44.39^{+0.07}_{-0.08}$	$44.30^{+0.06}_{-0.07}$	$44.40^{+0.10}_{-0.13}$	$44.58^{+0.15}_{-0.17}$	$44.35^{+0.14}_{-0.15}$	$43.85^{+0.32}_{-0.13}$	$44.87^{+0.08}_{-0.08}$	$44.90^{+0.16}_{-0.16}$	$45.04^{+0.12}_{-0.14}$	<44.28	$45.19^{+0.13}_{-0.14}$	0.22	0.58
IRAS 13218+0552	$45.54^{+0.07}_{-0.09}$	$45.96^{+0.15}_{-0.23}$	$46.02^{+0.13}_{-0.19}$	$45.74^{+0.15}_{-0.20}$	$45.87^{+0.20}_{-0.26}$	$45.70^{+0.21}_{-0.27}$	$46.32^{+0.13}_{-0.19}$	$46.32^{+0.18}_{-0.22}$	$46.55^{+0.16}_{-0.22}$	$45.58^{+0.22}_{-0.27}$	$46.63^{+0.16}_{-0.21}$	−0.59	−1.55
MCG –6-30-15	$43.19^{+0.05}_{-0.06}$	$43.16^{+0.07}_{-0.09}$	$43.23^{+0.04}_{-0.04}$	$43.23^{+0.06}_{-0.06}$	$43.18^{+0.06}_{-0.06}$	$43.04^{+0.05}_{-0.05}$	$43.72^{+0.05}_{-0.53}$	$43.69^{+0.06}_{-0.06}$	$43.83^{+0.06}_{-0.06}$	$43.05^{+0.06}_{-0.05}$	$44.02^{+0.05}_{-0.23}$	−0.19	−0.50
IC 4329A	$44.05^{+0.05}_{-0.05}$	$44.11^{+0.06}_{-0.07}$	$44.15^{+0.04}_{-0.04}$	$44.25^{+0.04}_{-0.04}$	$44.02^{+0.03}_{-0.03}$	$43.67^{+0.05}_{-0.05}$	$44.59^{+0.05}_{-0.35}$	$44.58^{+0.03}_{-0.04}$	$44.76^{+0.04}_{-0.04}$	$43.65^{+0.06}_{-0.06}$	$44.90^{+0.04}_{-0.16}$	0.08	0.21
H1419+480	$44.53^{+0.05}_{-0.05}$	$44.58^{+0.02}_{-0.03}$	$44.79^{+0.09}_{-0.11}$	$44.75^{+0.10}_{-0.13}$	$44.59^{+0.08}_{-0.10}$	$44.40^{+0.07}_{-0.83}$	$45.11^{+0.06}_{-0.06}$	$45.15^{+0.07}_{-0.18}$	$45.31^{+0.08}_{-0.10}$	<44.31	$45.40^{+0.11}_{-0.08}$	−0.05	−0.13
Mrk 478	$44.79^{+0.04}_{-0.04}$	$44.68^{+0.03}_{-0.03}$	$44.69^{+0.08}_{-0.09}$	$44.68^{+0.09}_{-0.11}$	$44.72^{+0.06}_{-0.06}$	$44.76^{+0.05}_{-0.04}$	$45.23^{+0.04}_{-0.07}$	$45.25^{+0.05}_{-0.08}$	$45.34^{+0.07}_{-0.07}$	$44.79^{+0.06}_{-0.10}$	$45.57^{+0.07}_{-0.07}$	−0.48	−1.26
H1537+339	$45.01^{+0.11}_{-0.16}$	$45.08^{+0.08}_{-0.08}$	$45.68^{+0.08}_{-0.52}$	<45.55	$45.34^{+0.08}_{-1.05}$	$45.16^{+0.05}_{-0.04}$	$45.78^{+0.10}_{-0.41}$	$45.94^{+0.08}_{-0.77}$	$46.08^{+0.04}_{-0.69}$	⋯	$46.18^{+0.08}_{-0.57}$	−0.11	−0.29
Kaz 102	$44.81^{+0.08}_{-0.10}$	$44.83^{+0.04}_{-0.05}$	$44.86^{+0.09}_{-0.10}$	$44.68^{+0.09}_{-0.18}$	<44.44	$43.97^{+0.08}_{-0.19}$	$45.33^{+0.06}_{-0.40}$	$45.03^{+0.08}_{-0.32}$	$45.35^{+0.07}_{-0.16}$	<44.18	$45.51^{+0.07}_{-0.15}$	0.08	0.21
E1821+643	$46.25^{+0.02}_{-0.02}$	$46.35^{+0.03}_{-0.03}$	$46.30^{+0.05}_{-0.05}$	$46.30^{+0.13}_{-0.16}$	$46.30^{+0.16}_{-0.19}$	$46.28^{+0.03}_{-0.30}$	$46.80^{+0.02}_{-0.60}$	$46.82^{+0.11}_{-0.19}$	$46.95^{+0.10}_{-0.10}$	$46.51^{+0.23}_{-0.74}$	$47.17^{+0.03}_{-0.41}$	−0.35	−0.92
H1834–653	$42.79^{+0.02}_{-0.02}$	$43.21^{+0.03}_{-0.03}$	$43.71^{+0.05}_{-0.05}$	$44.04^{+0.03}_{-0.02}$	$44.03^{+0.05}_{-0.02}$	$43.63^{+0.03}_{-0.05}$	$43.73^{+0.03}_{-0.81}$	$44.45^{+0.03}_{-0.03}$	$44.48^{+0.03}_{-0.12}$	$43.53^{+0.07}_{-0.07}$	$44.54^{+0.03}_{-0.12}$	−0.03	−0.08
Mrk 509	$44.43^{+0.04}_{-0.04}$	$44.46^{+0.03}_{-0.03}$	$44.40^{+0.05}_{-0.05}$	$44.46^{+0.07}_{-0.07}$	$44.44^{+0.09}_{-0.11}$	$44.34^{+0.06}_{-0.07}$	$44.94^{+0.04}_{-0.04}$	$44.94^{+0.07}_{-0.08}$	$45.08^{+0.06}_{-0.07}$	$44.31^{+0.06}_{-0.22}$	$45.24^{+0.06}_{-0.08}$	−0.32	−0.84
NGC 7213	$43.04^{+0.02}_{-0.02}$	$43.12^{+0.03}_{-0.04}$	$43.19^{+0.04}_{-0.05}$	$43.07^{+0.04}_{-0.05}$	$43.05^{+0.04}_{-0.04}$	$43.16^{+0.09}_{-0.09}$	<43.63	$43.63^{+0.05}_{-0.06}$	$43.75^{+0.04}_{-0.34}$	$43.38^{+0.10}_{-0.09}$	$43.98^{+0.05}_{-0.33}$	−0.52	−1.37
MR 2251–178	$44.59^{+0.11}_{-0.10}$	$44.56^{+0.06}_{-0.06}$	$44.55^{+0.06}_{-0.07}$	$44.41^{+0.10}_{-0.13}$	$44.38^{+0.11}_{-0.13}$	$44.32^{+0.05}_{-0.06}$	$45.10^{+0.09}_{-0.09}$	$44.92^{+0.08}_{-0.10}$	$45.12^{+0.08}_{-0.09}$	$44.43^{+0.04}_{-0.04}$	$45.34^{+0.09}_{-0.09}$	−0.36	−0.95
MCG –2-58-22	$44.50^{+0.08}_{-0.08}$	$44.59^{+0.06}_{-0.07}$	$44.62^{+0.05}_{-0.05}$	$44.38^{+0.06}_{-0.06}$	$44.16^{+0.05}_{-0.06}$	$43.91^{+0.06}_{-0.06}$	$45.09^{+0.07}_{-0.07}$	$44.77^{+0.06}_{-0.29}$	$45.09^{+0.05}_{-0.13}$	<44.04	$45.27^{+0.07}_{-0.14}$	−0.06	−0.16

NOTE.—$L(\lambda_1–\lambda_2)$ indicates logarithm of luminosity integrated between λ_1 and λ_2 (μm) in units of ergs s^{-1}. A cosmological model with $q_0 = 0$ and $H_0 = 50$ km s^{-1} Mpc^{-1} was used.

TABLE 6
OPTICAL, UV, AND X-RAY LUMINOSITIES

Name	$L(0.2–0.1\,\mu m)$	$L(0.4–0.2\,\mu m)$	$L(0.8–0.4\,\mu m)$	$L(1.6–0.8\,\mu m)$	$L(0.1–2.0\,keV)$	$L(2–10\,keV)$	L_{bol} (1 mm–10 keV)
Mrk 1152	$43.00^{+0.01}_{-0.01}$	$42.96^{+0.00}_{-0.00}$	$43.63^{+0.00}_{-0.00}$	$44.22^{+0.11}_{-0.11}$	$44.13^{+0.14}_{-0.13}$	$44.11^{+0.11}_{-0.14}$	$45.19^{+0.10}_{-0.11}$
Mrk 590	$44.36^{+0.05}_{-0.05}$	$44.20^{+0.04}_{-0.04}$	$44.23^{+0.01}_{-0.02}$	$43.86^{+0.02}_{-0.02}$	$44.05^{+0.20}_{-0.20}$	$43.61^{+0.14}_{-0.14}$	$45.16^{+0.09}_{-0.14}$
ESO 198−G24	$43.99^{+0.10}_{-0.14}$	$43.76^{+0.04}_{-0.06}$	$43.78^{+0.00}_{-0.01}$	$44.02^{+0.01}_{-0.01}$	$44.77^{+0.04}_{-0.03}$	. . .	$45.29^{+0.07}_{-0.11}$
3A 0557−383	$43.26^{+0.08}_{-0.13}$	$43.52^{+0.11}_{-0.16}$	$43.79^{+0.13}_{-0.20}$	$44.07^{+0.14}_{-0.21}$	$42.95^{+0.01}_{-0.01}$	$43.89^{+0.09}_{-0.10}$	$45.31^{+0.09}_{-0.12}$
PG 0804+761.............	$45.53^{+0.22}_{-0.20}$	$45.47^{+0.04}_{-0.04}$	$45.01^{+0.02}_{-0.03}$	$44.83^{+0.04}_{-0.05}$	$44.82^{+0.27}_{-0.22}$	$44.53^{+0.10}_{-0.10}$	$46.27^{+0.14}_{-0.12}$
H1039−074.................	$46.02^{+0.01}_{-0.01}$	$45.96^{+0.01}_{-0.01}$	$45.72^{+0.02}_{-0.02}$	$45.57^{+0.02}_{-0.03}$	. . .	. . .	$47.38^{+0.11}_{-0.04}$
NGC 3783...................	$43.88^{+0.01}_{-0.01}$	$44.02^{+0.01}_{-0.01}$	$43.82^{+0.02}_{-0.02}$	$43.20^{+0.02}_{-0.02}$	$42.95^{+0.11}_{-0.08}$	$43.18^{+0.10}_{-0.10}$	$44.86^{+0.02}_{-0.02}$
Ton 1542....................	$44.99^{+0.02}_{-0.03}$	$44.84^{+0.03}_{-0.03}$	$44.47^{+0.04}_{-0.06}$	$44.39^{+0.09}_{-0.10}$	$44.62^{+0.05}_{-0.05}$	$43.90^{+0.05}_{-0.05}$	$45.75^{+0.07}_{-0.07}$
IRAS 13218+0552	$44.25^{+0.06}_{-0.01}$	$44.11^{+0.07}_{-0.02}$	$44.33^{+0.17}_{-0.11}$	$44.68^{+0.08}_{-0.03}$	$46.01^{+0.00}_{-0.00}$	$45.75^{+0.00}_{-0.00}$	$46.74^{+0.13}_{-0.15}$
MCG −6-30-15...........	< 42.87	$42.73^{+0.02}_{-0.68}$	$43.24^{+0.01}_{-0.01}$	$43.23^{+0.02}_{-0.02}$	$43.39^{+0.21}_{-0.21}$	$42.87^{+0.04}_{-0.04}$	$44.29^{+0.10}_{-0.27}$
IC 4329A	$43.27^{+0.01}_{-0.01}$	$43.29^{+0.01}_{-0.01}$	$43.83^{+0.01}_{-0.01}$	$43.96^{+0.02}_{-0.02}$	$43.73^{+0.04}_{-0.04}$	$43.75^{+0.09}_{-0.10}$	$45.05^{+0.14}_{-0.12}$
H1419+480.................	$44.06^{+0.10}_{-0.06}$	$44.27^{+0.10}_{-0.05}$	$44.33^{+0.13}_{-0.07}$	$44.32^{+0.15}_{-0.08}$	$44.05^{+0.05}_{-0.05}$	$44.79^{+0.03}_{-0.04}$	$45.59^{+0.10}_{-0.07}$
Mrk 478	$45.11^{+0.10}_{-0.12}$	$44.80^{+0.03}_{-0.03}$	$44.64^{+0.02}_{-0.03}$	$44.63^{+0.04}_{-0.05}$	$44.75^{+0.16}_{-0.16}$	$44.27^{+0.06}_{-0.08}$	$45.98^{+0.09}_{-0.10}$
H1537+339.................	$45.01^{+0.26}_{-0.23}$	$45.19^{+0.13}_{-0.12}$	$45.22^{+0.07}_{-0.08}$	$45.12^{+0.09}_{-0.12}$	$44.93^{+0.50}_{-0.32}$	$46.49^{+0.00}_{-0.00}$	$46.72^{+0.08}_{-0.15}$
Kaz 102......................	$45.53^{+0.03}_{-0.03}$	$45.33^{+0.02}_{-0.02}$	$44.87^{+0.04}_{-0.06}$	$44.66^{+0.08}_{-0.07}$	$44.37^{+0.11}_{-0.52}$	. . .	$46.14^{+0.11}_{-0.12}$
E1821+643	$46.22^{+0.12}_{-0.12}$	$46.43^{+0.03}_{-0.03}$	$46.18^{+0.01}_{-0.01}$	$46.15^{+0.01}_{-0.01}$	$45.85^{+0.31}_{-0.26}$	$45.86^{+0.02}_{-0.02}$	$47.46^{+0.00}_{-0.35}$
H1834−653	$42.11^{+0.02}_{-0.02}$	$42.07^{+0.01}_{-0.01}$	$43.04^{+0.01}_{-0.02}$	$42.96^{+0.01}_{-0.01}$	$43.40^{+0.34}_{-0.30}$	$43.10^{+0.08}_{-0.09}$	$44.60^{+0.04}_{-0.11}$
Mrk 509	$45.20^{+0.04}_{-0.04}$	$45.08^{+0.03}_{-0.03}$	$44.56^{+0.01}_{-0.01}$	$44.31^{+0.05}_{-0.05}$	$44.89^{+0.06}_{-0.06}$	$44.38^{+0.10}_{-0.10}$	$45.92^{+0.05}_{-0.06}$
NGC 7213...................	$42.58^{+0.01}_{-0.00}$	$42.62^{+0.01}_{-0.00}$	$42.89^{+0.01}_{-0.01}$	$42.95^{+0.01}_{-0.01}$	$42.91^{+0.06}_{-0.03}$	$42.64^{+0.15}_{-0.14}$	$44.15^{+0.04}_{-0.21}$
MR 2251−178	$45.16^{+0.11}_{-0.11}$	$45.00^{+0.10}_{-0.10}$	$44.75^{+0.03}_{-0.03}$	$44.66^{+0.11}_{-0.11}$	$44.52^{+0.30}_{-0.27}$	$44.54^{+0.03}_{-0.03}$	$45.88^{+0.12}_{-0.11}$
MCG −2-58-22...........	$44.92^{+0.07}_{-0.08}$	$44.71^{+0.07}_{-0.09}$	$44.52^{+0.14}_{-0.30}$	$44.58^{+0.11}_{-0.17}$	$44.52^{+0.27}_{-0.26}$	$44.65^{+0.09}_{-0.09}$	$45.72^{+0.12}_{-0.15}$

NOTE.—Values are logarithm of luminosity in units of ergs s^{-1}. A cosmological model with $q_0 = 0$ and $H_0 = 50$ km s^{-1} Mpc^{-1} was used.

sufficient counts to measure the soft X-ray slope. These objects were also chosen to be optically bright enough to be observed by *IUE*. The sample is low-redshift, heterogeneous, half radio-and half optically selected, and biased toward AGNs with strong soft X-ray to optical flux ratios.

The *HEAO* and E94 samples have similar redshift ranges ($0 < z < 0.35$). We found (comparing our Tables 5 and 6 and their Tables 15 and 16) that the range of IR and optical luminosities is similar in both samples, while the UV and soft and hard X-ray luminosities of the *HEAO* sample extend to lower values (see also Fig. 4). We compared the distributions of various IR, optical, and UV octave luminosity ratios (optical/near-IR, UV/near-IR, optical/UV, and IR/IR) between the two samples and found that only

the luminosity ratios $L(0.2–0.4\ \mu m)/L(0.4–0.8\ \mu m)$ and $L(0.2–0.4\ \mu m)/L(0.8–1.6\ \mu m)$ differ (see Fig. 5). The K-S test shows a less than 1% probability that the *HEAO* and E94 samples have the same distributions for these luminosity ratios. The *HEAO* sample extends to lower $L(0.2–0.4\ \mu m)/L(0.4–0.8\ \mu m)$ and $L(0.2–0.4\ \mu m)/L(0.8–1.6\ \mu m)$ ratios, meaning that it includes objects with redder optical/UV continua. This finding is also confirmed when the

FIG. 2.—Median energy distributions for our sample normalized at 1.5 μm and the 68, 90, and 100 (*dashed line*) Kaplan-Meier percentile envelopes.

TABLE 7
DUST TEMPERATURE RANGE

Name	T_{min}	T_{max}	α_{cut}[a]
Mrk 1152	<30	1000	. . .
Mrk 590[b]............................	20	1000	. . .
ESO 198−G24	40	1000	0.2
3A 0557−383	20	1000	0.7
PG 0804+761......................	40	1000	0.6
H1039−074..........................	40	500	. . .
NGC 3783...........................	30	1000	1.4
Ton 1542.............................	<80	1000	. . .
IRAS 13218+0552	50	1000	1.8
MCG −6-30-15	40	1000	1.3
IC 4329A	40	1000	0.8
H1419+480..........................	40	1000	0.3
Mrk 478	40	1000	1.8
H1537+339.........................	<40	500	. . .
KAZ 102..............................	40	1000	0.2
E1821+643	40	1000	2.5
H1834−653	50	1000	1.6
Mrk 509	40	1000	2.2
NGC 7213[b].........................	<20	1000	. . .
MR 2251−178	40	1000	3.7
MCG −2-58-22....................	40	1000	2.5

[a] Values of α_{cut} indicate the far-IR cutoff slope.
[b] The SED is unusually flat and covers the full range of observable temperatures; no strong constraints on temperature can be placed.
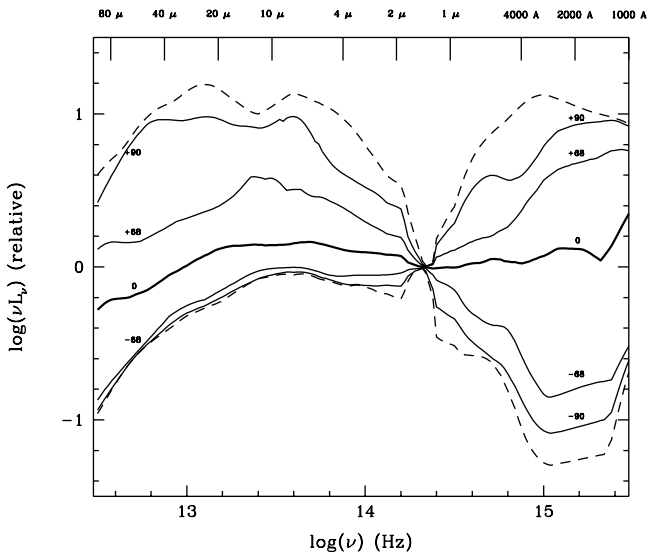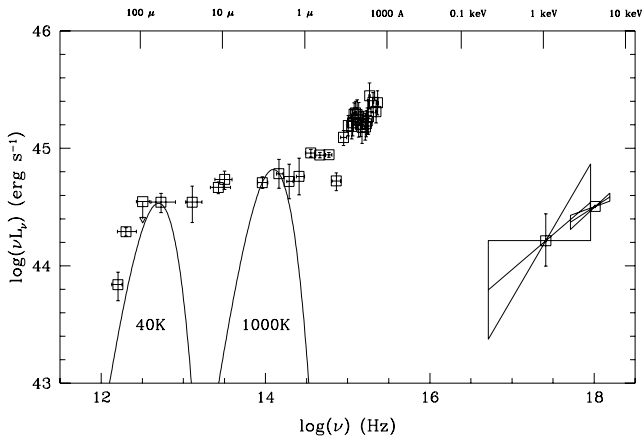
FIG. 3.—Dust temperature range in MR 2251−178

median energy distribution of the *HEAO* sample is compared with that of E94 (see our Fig. 2 and their Fig. 11*a*). The discrepancy is strongest at the bluest wave bands, suggesting that dust absorption may be the cause. In this case, the range of the $L(0.2–0.4\,\mu m)/L(0.4–0.8\,\mu m)$ and $L(0.2–0.4\,\mu m)/L(0.8–1.6\,\mu m)$ ratios indicates that $\sim$30%–40% of the sample are reddened at levels of $E(B–V) \geq 1.2$ and may have been missed by other surveys.

To understand the relation between the X-ray–selected sources and those from other samples, we compare (Fig. 6) the $B–K$ colors of the *HEAO* subset analyzed here (*shaded area*) with the full *HEAO* AGN sample (*dotted-line–shaded area*), the radio-selected quasars from Webster et al. (1995; *solid line*), optically selected PG QSOs from Neugebauer et al. (1987; *dash-dotted line*), and the *Chandra*-observed subset of the 2 μm All Sky Survey (2MASS) AGNs from Wilkes et al. (2002). The radio and hard X-ray–selected samples show the widest range of colors, although the radio-selected sources have a larger proportion of blue sources (a one-tailed K-S test gave a 99.5% significance; the means are 3.34 and 4.03, while the $B–K$ medians are 3.1 and 3.99 for the radio and full *HEAO* samples, respectively), similar to the

very narrow range of the optically selected PG sources. The PG quasars have the bluest distribution: a one-tailed K-S test gave $\geqslant$99.9% probability that the PG distribution is bluer than the radio, *HEAO*, and 2MASS distributions, respectively, which is also evident when the $B–K$ means are compared: 0.74 (PG) with 3.34 (radio), 4.03 (full *HEAO*), 5.60 (2MASS), and $B–K$ medians: 0.72 (PG) with 3.1 (radio), 3.99 (full *HEAO*), 5.48 (2MASS). The red 2MASS AGNs, selected by their red near-IR colors, largely overlap the red end of the radio and hard X-ray–selected samples, implying that both these selection techniques include similar, red AGNs.

Although we cannot determine the $B–K$ distribution of the intrinsic AGN population from this comparison, Figure 6 clearly demonstrates the large discrepancies between samples selected in different wave bands (a two-tailed K-S test showed that the distributions of the PG, *HEAO*, 2MASS, and Webster et al. radio samples have different distributions at the $\geqslant$99.5%). It is clear that radio and hard X-ray samples cover a much wider range of optical colors than optically selected samples. It is also notable that the peak in the distribution of $B–K$ colors for the hard X-ray–selected sources is significantly redder than that of the radio-selected sample (a one-tailed K-S test gave $\geqslant$99.5% significance). This indicates either a lack of blue AGNs in the hard X-ray sample, which seems unlikely given that these are the easiest AGNs to find and classify, or a lack of red AGNs in the radio sample. Such a lack could be due to differing classification schemes for radio and X-ray–selected sources preferentially excluding more of the reddest sources in the radio sample, e.g., because of the lack of broad optical emission lines.

4. IMPLICATIONS FOR THE STRUCTURE OF ACTIVE GALACTIC NUCLEI

4.1. *A Comparison of Dust (Optical) versus Gas (X-Ray) Absorption Column Densities*

If the redder $B–K$ colors indicate more dust obscuration, as suggested by Webster et al. (1995), then the above
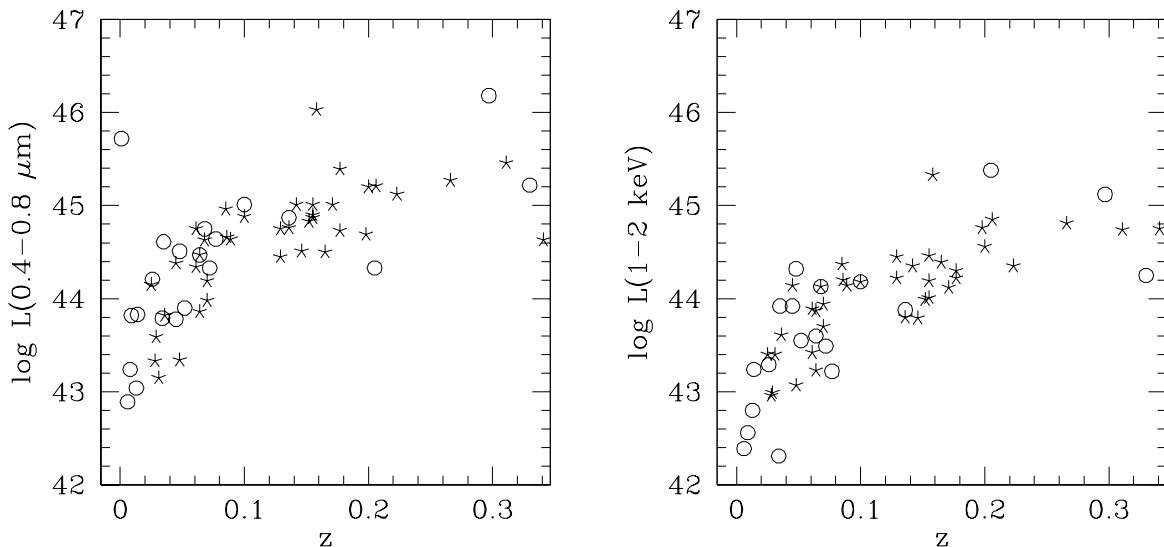
FIG. 4.—Relation between luminosity and redshift. Open circles indicate our sample, and stars indicate the Elvis et al. (1994) sample.
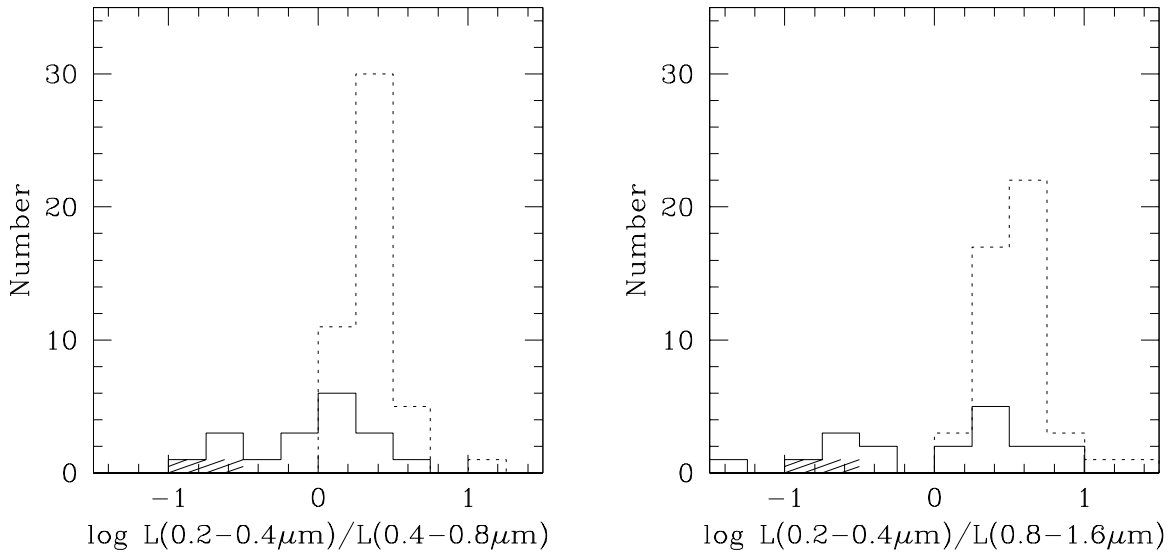
Fig. 5.—Histograms of $L(0.2–0.4\ \mu m)/L(0.4–0.8\ \mu m)$ and $L(0.2–0.4\ \mu m)/L(0.8–1.6\ \mu m)$. Our sample is represented by a solid line, while the Elvis et al. (1994) sample is represented by a dotted line. We have excluded 3A 05574−383, H1419+480, and H1537+339 from the histograms, as these objects did not have enough data points in the 0.2–0.4 μm wavelength range to calculate the luminosity. Hatched regions represent IC 4329A and H1834−653, which have intrinsic $N_{\rm H}$.

findings suggest that the *HEAO* sample includes a larger proportion of dust-obscured AGNs than either optically or radio-selected samples, which miss perhaps as many as ∼30%–40% of the population. The availability of both optical and X-ray data for many of these sources allows us to investigate the properties and structure of both the dust and the gas in the obscuring material. It is well-established that AGNs show a smaller amount of optical dust absorption than indicated by the X-ray (gas) absorption if a " normal "

gas-to-dust ratio is assumed (Maiolino et al. 2001; Risaliti et al. 2000). The ratio varies from factors of a few to 2–3 orders of magnitude. A number of explanations have been suggested, such as abnormal gas-to-dust ratios, largely dust-free gas, dust in the form of large grains whose opacity is not a strong function of wavelength, and differing lines of sight and corresponding absorption column densities toward the optical and X-ray emission regions.

A subset of the sources in the current sample have sufficient data to make a comparison. Those objects with known intrinsic X-ray absorption, are 3A 05574−383 (a Seyfert 1 with $N_{\rm H} = 7 \times 10^{21}$ cm^{-2}), IC 4329A (a Seyfert 1.2 with $N_{\rm H} = 1.5 \times 10^{21}$ cm^{-2}), and H1834−653 (a Seyfert 2 with $N_{\rm H} = 13.5 \times 10^{22}$ cm^{-2}). Other AGNs show either no evidence of intrinsic X-ray absorption or no information is available for them (see Table 3). As dust is generally associated with gas, objects with intrinsic $N_{\rm H}$ are expected to show redder optical/UV spectra. Indeed those objects with intrinsic $N_{\rm H}$ show the lowest $L(0.2–0.4\ \mu m)/L(0.4–0.8\ \mu m)$ and $L(0.2–0.4\ \mu m)/L(0.8–1.6\ \mu m)$ ratios (see Fig. 5, where the high intrinsic $N_{\rm H}$ objects are represented by hatched regions). To estimate the amount of intrinsic dust absorption, we took the observed SEDs (previously corrected for Galactic extinction) and dereddened them by $E(B-V)$ values ranging from 0.1 to 1.5 in steps of 0.1. The smallest $E(B-V)$ that produced an SED with a big blue bump showing no downturns in the optical/UV was taken as a lower limit estimate of the intrinsic absorption for that object. For IC 4329A and H1834−653 the $E(B-V)$ was estimated to be ≥1.2 and ≥1.1, respectively, which translates to $N_{\rm H} = 6 \times 10^{21}$ and 5.5×10^{21} cm^{-2}, assuming the standard conversion of $N({\rm H\ I})/E(B-V) = 5 \times 10^{21}$ cm^{-2} for the Galactic dust/gas ratio (Diplas & Savage 1994; 3A 05574−383 has too few optical/UV data points to estimate the big blue bump shape). A comparison of absorption estimated from the optical/UV (above) and X-rays (Table 3) shows a ∼4 times higher and a 30 times lower dust/gas ratio for IC 4329A and H1834−653, respectively. A higher/lower
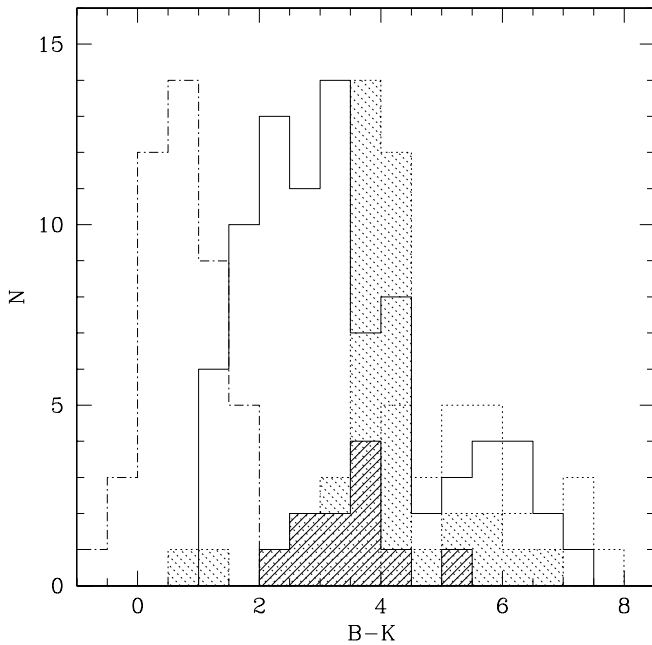

Fig. 6.—Comparison of $B-K$ colors between the *HEAO* sample (*dotted-line–shaded area*), the *HEAO* subsample analyzed in this paper (*solid-line–shaded area*), the Webster et al. sample (*solid line*), the PG sample (*dash-dotted line*), and the *Chandra*-observed 2MASS sample (*dotted line*).

dust-to-gas ratio can be explained by either smaller/larger dust grains or the presence of an ionized absorber (see below) in the objects with higher dust-to-gas ratios.

In our sample we also find objects that are extremely red in the optical/UV wavelength range, with nonexistent big blue bumps [where $L(0.2–0.4 \ \mu m)/L(0.4–0.8 \ \mu m)$ and $L(0.2–0.4 \ \mu m)/L(0.8–1.6 \ \mu m)$ is less than -0.5] but normal X-ray softness ratio [$L(0.5–2 \ keV)/L(2–10 \ keV) \geq 0$] and steep ($\Gamma > 1$) soft X-ray slopes, indicating no or little intrinsic X-ray absorption from neutral gas. These include Mrk 1152 (Seyfert 1.5) and MCG -6-30-15 (Seyfert 1.2). The lower limits for $E(B-V)$ estimated from the downturn of the big blue bump in the optical/UV range are 1.2 and 1.6, for Mrk 1152 and MCG -6-30-15, respectively. This translates to H I column densities of 6×10^{21} and 8×10^{21} cm^{-2}, respectively (assuming a Galactic dust/gas ratio), which should result in detectable soft X-ray absorption in the spectra of these objects. MCG -6-30-15 is known to have a dusty warm absorber (Reynolds 1997), which can explain the lack of soft X-ray absorption via neutral gas combined with the reddening in optical/UV via dust. Since Mrk 1152 shows similar optical/UV/X-ray SED properties to MCG -6-30-15, it may be a candidate for a dusty warm absorber. However, detailed X-ray spectral analysis is needed to confirm this and rule out smaller than Galactic dust grains as another option.

In addition, IC 4329A, noted above to show X-ray absorption, but with a dust-to-gas ratio a few times higher than the Galactic value, can also be explained if some of the absorbing gas is ionized. The X-ray spectrum of this object, observed by *BeppoSAX* (Perola et al. 1999), shows comparable column densities of both cold and warm absorption (the latter indicated by the ~ 0.7 keV feature corresponding to the O VI and O VII blend) and so is consistent with our interpretation.

To obtain a more general view of the sample we plot (Fig. 7) the X-ray softness ratio, i.e., the $L(0.1–2 \ keV)/L(2–10 \ keV)$ as a function of the big blue bump shape indicated by the following UV/optical/near-IR luminosity ratios: $L(0.2–0.4 \ \mu m)/L(0.4–0.8 \ \mu m)$ and $L(0.2–0.4 \ \mu m)/L(0.8–1.6 \ \mu m)$. AGNs with high ($>0$) $L(0.2–0.4 \ \mu m)/L(0.4–0.8 \ \mu m)$ and $L(0.2–0.4 \ \mu m)/L(0.8–1.6 \ \mu m)$ ratios, which are also comparable to the luminosity ratios of the soft X-ray–selected sample of E94 (see Fig. 5), are those with pronounced and unabsorbed big blue bumps, and include mostly (with the exception of Mrk 509, a Seyfert 1.2, and MCG -2-58-22, a Seyfert 1.5) Seyfert 1 galaxies (Fig. 8, *open circles*). AGNs with ratios less than 0 and smaller than E94 are mostly intermediate-type (Seyfert 1.2 and 1.5) and type 2 Seyfert galaxies (Fig. 7, *filled circles*). This finding is broadly consistent with unified models of AGNs in which Seyfert 1 galaxies are viewed face on to a dusty torus-like structure, and hence their continua are expected to be less absorbed and bluer than the continua of the intermediate type and type 2 Seyfert galaxies, which are viewed at larger (more edge-on) inclination angles and are more absorbed. Objects with low X-ray softness ratios (<-0.5) in Figure 7, indicative of neutral gas absorption, include H1834-653 (a heavily absorbed Seyfert 2), 3A 05574$-$383 (a Seyfert 1 with considerable N_H; see Table 3), H1537+339 (a Seyfert 1), and H1419+480 (a Seyfert 1 for which no indication of intrinsic N_H has been found in the literature). Unfortunately for almost all of these objects (with the exception of the H1834-653), the SEDs in the 0.2–0.4 μm and UV wavelength range lack data points, so the values of $L(0.2–0.4 \ \mu m)/L(0.4–0.8 \ \mu m)$ and $L(0.2–0.4 \ \mu m)/L(0.8–1.6 \ \mu m)$ ratios in Figure 7 are uncertain. We can, however, predict the direction (*horizontal arrows*) in which the SED would move if the UV points were available based on the blue bump shape in the optical. Objects that lack soft X-ray data, i.e., those which have uncertain softness ratios, are indicated by vertical arrows. We also plot in Figure 7 the dependence of UV/optical colors and X-ray softness ratio on N_H. It is apparent that the UV/optical colors can be explained by a lower N_H range, than is needed to explain the X-ray softness range.
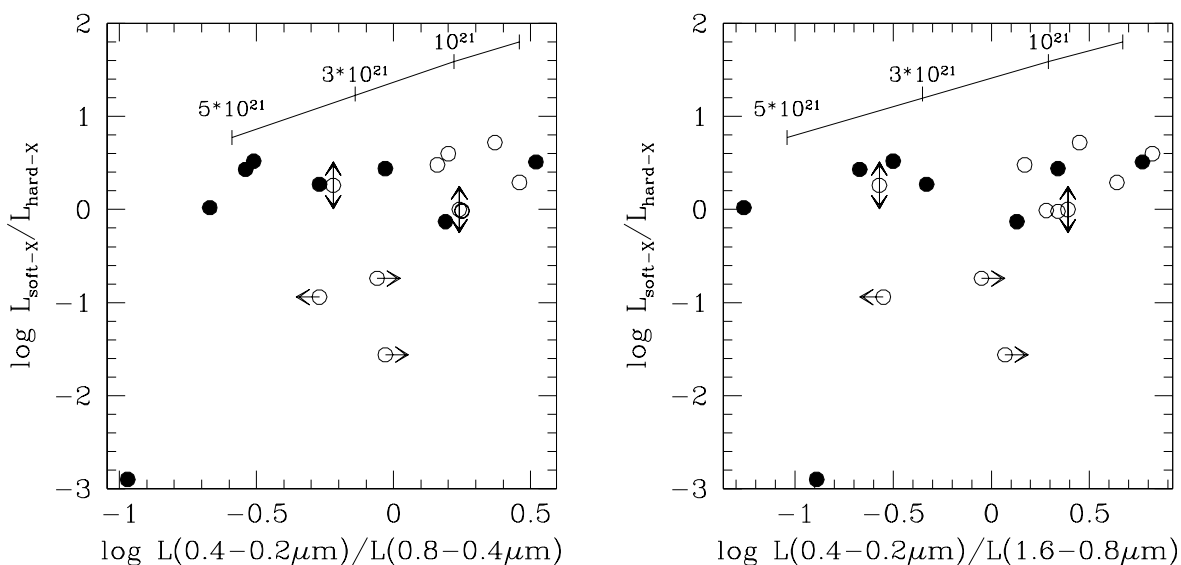

FIG. 7.—X-ray softness ratio vs. $L(0.2–0.4 \ \mu m)/L(0.4–0.8 \ \mu m)$ and $L(0.2–0.4 \ \mu m)/L(0.8–1.6 \ \mu m)$ ratios. Circles with horizontal arrows represent 3A 05574$-$383, H1419+480, and H1537+339, which do not have enough data points to calculate the 0.2–0.4 μm luminosity, so their position with respect to the X-axis is not well defined. Vertical arrows indicate objects with ratios that are uncertain because of a lack of soft X-ray data. Open circles are Seyfert 1 galaxies, and filled circles are intermediate and type 2 Seyfert galaxies. The Galactic dust reddening curve for different column densities N_H is shown.
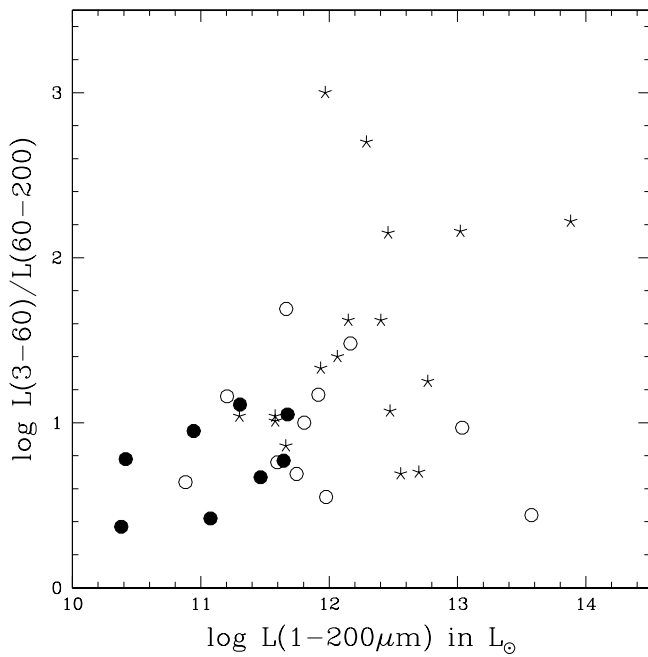
FIG. 8.—Ratio of warm (3–60 μm) to cool (60–200 μm) IR luminosity plotted as a function of the total IR luminosity for the *HEAO* sample (intermediate and type 2 AGNs: *filled circles*; type 1 AGNs: *open circles*) and the Polletta et al. sample of type 1 AGNs (*stars*).

4.2. *Diagnostics from the IR Continuum*

The relative contribution of emission in the warm (mid-IR [$\sim$25 μm]) and cool (far-IR [$\sim$60–100 μm]) IR potentially provides an important diagnostic of the energy sources responsible. The relative strength of the mid- to far-IR emission correlates with that of an active nucleus (de Grijp et al. 1985; Heisler & De Robertis 1999). In the popular, two-component thermal dust model for AGN IR emission (Rowan-Robinson & Crawford 1989; Rowan-Robinson 1995), the AGN heats dust close to the nucleus generating mid-IR emission in addition to the far-IR emission from a ubiquitous starburst component. As we have seen, a popular model for the AGN IR component is reemission from an optically thick dusty torus (Pier & Krolik 1992; Granato & Danese 1994) that unifies type 1 and type 2 AGNs via obscuration of the central AGN by the edge-on torus in the latter. The torus optical depths are sufficiently high ($N_{\rm H} \sim 10^{24}$ cm^{-2}) that the SED of the AGN IR component is a strong function of viewing angle or, equivalently, the column density of obscuring material along our line-of-sight through the material. It is likely that both AGN luminosity and the amount of line-of-sight obscuration contribute to the mid-IR SED shape, combined with the relative strength of the host galaxy emission at the lower luminosity end (Lumsden et al. 2001; Alexander 2001).

We determine the luminosities of the *HEAO* sample in the warm 3–60 μm band and cold 60–200 μm bands (Table 5) and compare this ratio with those for the quasar sample of Polletta et al. (2000), which includes both radio-loud and radio-quiet quasars with SEDs of similar quality to ours. The resulting ratio of warm to cool IR emission is plotted in Figure 8 as a function of the total IR luminosity for both samples. The distribution suggests that the *HEAO* sample lacks objects with large $L(3$–60 μm$)/L(60$–200 μm$)$ ratios, i.e., those with the largest AGN contribution, although this

difference is only marginally significant for the samples as a whole (the K-S test gave a 5% probability that the two samples have the same distribution). Since the nonthermal radio emission has been subtracted from the IR spectra of the Polletta et al. (2000) quasars, and objects with larger $L(3$–60 μm$)/L(60$–200 μm$)$ ratios are either radio-quiet or radio-intermediate, any difference cannot be due to the contribution of radio-linked, nonthermal emission in their radio-loud quasars. Those objects with the largest AGN contribution, $L(3$–60 μm$)/L(60$–200 μm$) > 1.7$, are those with the highest total IR luminosity supporting a scenario where the far-IR emission is associated with a starburst in the host galaxy that is more dominant for the lower luminosity and/or intermediate-type sources of which the *HEAO* sample includes a larger proportion.

In Table 5 we also present a widely-used alternative measure of warm to cool IR emission, the ratio between the 25 and 60 μm flux, and compare (Fig. 9) the *HEAO* sample with the soft X-ray sample of E94, Seyfert galaxies (including types 1 and 2) from de Grijp et al. (1985) and Low et al. (1988), and the Palomar-Green QSOs from Sanders et al. (1989). In this figure we also mark the ratio characteristic for normal spiral galaxies in the Virgo Cluster from Soifer, Neugebauer, & Houck (1987). The *HEAO* 25/60 ratios extend toward warmer colors when compared to Seyfert galaxies but are consistent with the IR colors of QSOs and the E94 sample. Although one object (3A 0557−385) in the *HEAO* sample has a larger 25/60 ratio than the E94 sample, and E94 AGNs extend toward smaller ratios, the distribution of the 25/60 ratios is statistically indistinguishable in *HEAO* and E94 samples (K-S test gives a 84% probability that the samples are drawn from the same population).
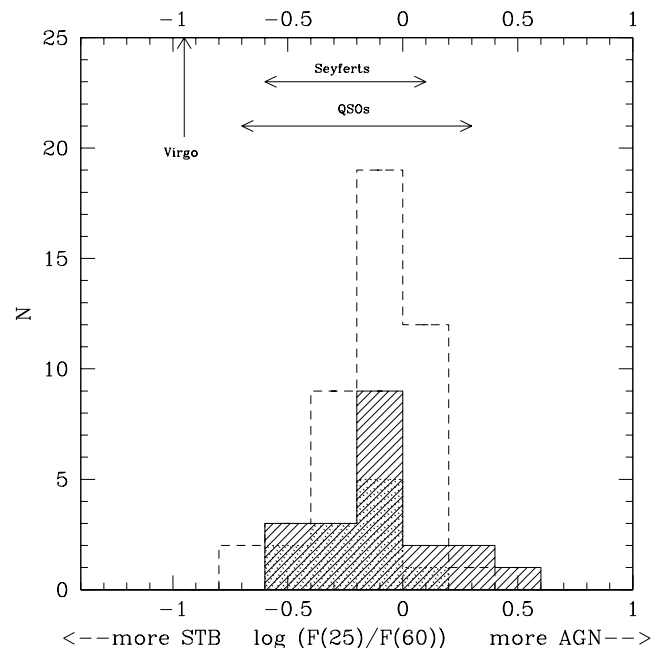

FIG. 9.—Comparison of the distribution of the 25/60 μm flux ratio of the *HEAO* sample (*shaded histogram*). The reddest objects, with $L(0.2$–0.4 μm$)/L(0.4$–0.8 μm$) < 0$ are indicated by the dotted-line–shaded areas. The E94 sample is indicated by the dashed-line histogram, the range presented in Seyfert 1 and 2 galaxies is from de Grijp et al. (1985) and Low et al. (1988), and the Palomar-Green QSOs are from Sanders et al. (1989). The 25/60 ratio for normal spiral galaxies from the Virgo Cluster from Soifer et al. (1987) is indicated by "Virgo."
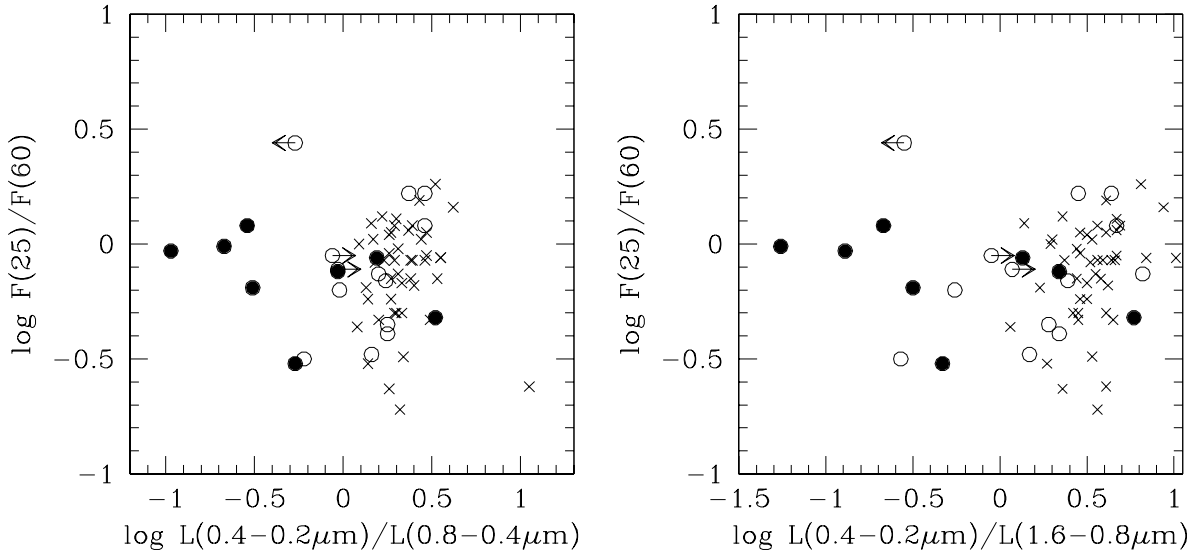
Fig. 10.—25/60 μm flux ratios vs. the UV/optical reddening indicators. Open circles are *HEAO* Seyfert 1 galaxies, filled circles are *HEAO* Seyfert 1.2, 1.5, and 2 galaxies, and crosses are E94 quasars.

If obscuration is a significant contributor to the 25/60 μm flux ratio, then we would expect some difference between these distributions for the *HEAO* and E94 samples. We showed in § 3.2 that the *HEAO* sample includes more optically reddened AGNs than the E94 sample, with half of the *HEAO* AGNs showing lower UV/optical ratios, i.e., $L(0.2–0.4 \mu m)/L(0.4–0.8 \mu m)$ and $L(0.2–0.4 \mu m)/L(0.8–1.6 \mu m)$, than the E94 AGNs. We plot in Figure 10 the relation between 25/60 ratio and the UV/optical ratio: $L(0.2–0.4 \mu m)/L(0.4–0.8 \mu m)$ and $L(0.2–0.4 \mu m)/L(0.8–1.6 \mu m)$. The *HEAO* AGNs with $L(0.2–0.4 \mu m)/L(0.4–0.8 \mu m) < 0$ are mostly intermediate and type 2 Seyfert galaxies. No correlation between the 25/60 ratio and the dust indicator from the UV/optical SED is present, the more reddened Seyfert galaxies, with $L(0.2–0.4 \mu m)/L(0.4–0.8 \mu m) < 0$, do not show larger 25/60 ratios than the blue [i.e., $L(0.2–0.4 \mu m)/L(0.4–0.8 \mu m) > 0$] Seyfert galaxies (K-S test showed a less than 30% probability that the two distributions are different). The combination of redder optical colors and lack of a difference in the mid-IR indicates $N_H \sim 10^{22}$ cm^{-2}. This is inconsistent with torus models implying an obscuring structure that is less optically thick, at least along the lines of sight represented here.

In Figure 11 we present the relation between 12/60 and 25/60 ratios and represent the *HEAO* Seyfert 1 galaxies as open circles, *HEAO* intermediate-type Seyfert galaxies as filled circles, Seyfert 2 galaxies as a filled square, and the E94 AGNs as crosses. We also include from Heisler, Lumsden, & Bailey (1997) the Seyfert 2 galaxies with a hidden broad-line region (HBLR), i.e., Seyfert 2 galaxies that show broad emission lines in polarized light and Seyfert 2 galaxies without a hidden broad-line region (non-HBLR), i.e., Seyfert 2 galaxies that do not show broad emission lines in polarized light. This correlation between the 12/60 and 25/60 ratios in HBLR and non-HBLR Seyfert 2 galaxies was initially interpreted by Heisler et al. (1997) within the context of unified schemes, such that Seyfert 2 galaxies with no HBLR are viewed edge-on to the torus, which obscures the mid-IR emission and hides the scattering medium producing polarized broad emission lines, while the Seyfert 2

galaxies with HBLR are viewed from angles skimming the dusty obscuring structure, large enough to hide the broad-line region and small enough to see the warm 25 μm dust emission and the scattering medium (see also Tran 2003, who finds hotter circumnuclear dust temperatures and mid-IR spectra more characteristic of Seyfert 1 galaxies in HBLR Seyfert 2 galaxies compared to non-HBLR Seyfert 2 galaxies). This simple picture was later modified to include the significant effects of the host galaxy in the non-HBLR Seyfert 2 galaxies, which tend to have lower overall
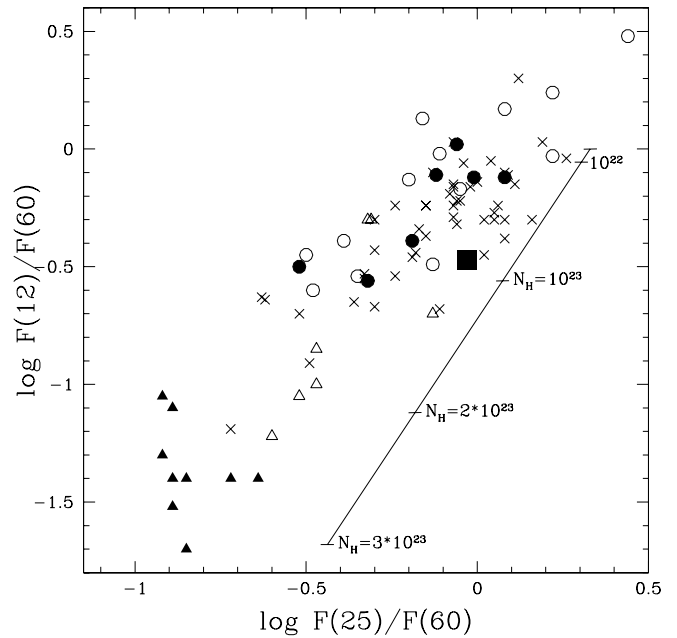

Fig. 11.—12/60 vs. 25/60 μm flux ratios. Seyfert 1 galaxies from the *HEAO* sample are represented by open circles, intermediate-type Seyfert galaxies by filled circles, and the type 2 Seyfert galaxy by a filled square. Filled crosses show the E94 sample, open triangles show Seyfert 2 galaxies with a hidden broad-line region, and filled triangles show Seyfert 2 galaxies without a hidden broad-line region from Heisler et al. 1997.

luminosity (Alexander 2001; Lumsden et al. 2001). The *HEAO* and E94 AGNs extend the non-HBLR and HBLR Seyfert 2 correlation toward warmer 25/60 and 12/60 ratios roughly along a reddening curve for Galactic dust. This general trend again points toward a modified unified scheme including an obscuring structure that is less optically thick than a torus and whose column density decreases more smoothly toward more face-on viewing angles.

In Figure 11 there is a region, at colors suggesting $N_H \sim 10^{23}$ cm^{-2} according to the Galactic reddening curve shown, where there is overlap between the reddest type 1 AGNs from both the E94 and the *HEAO* sample, intermediate types from the *HEAO* sample, and the HBLR Seyfert 2 galaxies from Heisler, Lumsden, & Bailey (1997). In this scenario, in which the viewing angles are similar for these objects, such a mix could be achieved via differing lines of sight to the BLR and the various continuum emitting regions. An alternative is to invoke a clumpy distribution of dust, where the Seyfert 1–1.5 galaxies in the *HEAO* sample are viewed through holes, while the HBLR Seyfert 2 galaxies are totally obscured.

Looking at a few of the individual cases could prove instructive here. Along with two HBLR Seyfert 2 galaxies, the spectroscopically classified Seyfert 2 H1834−653 has a warm 25/60 ratio of −0.03, more consistent with the colors of Seyfert 1 galaxies. It is one of the lowest luminosity sources in our sample with a high host galaxy/AGN ratio (see Tables 5 and 3), so the AGN-like appearance of its mid-IR colors cannot be explained by an unusually dominant AGN in the IR. However, the amount of reddening needed to explain the red optical/UV SED is $\sim E(B−V) = 1.1$ (§ 4.1), which corresponds to a negligible extinction of 0.05 mag at 25 μm and 0.007 mag at 60 μm, is likely sufficient to allow the galaxy light to dominate the optical/UV emission and thus to lose the BLR. Alternatively the obscuring material could lie in the host galaxy, as in IC 4329A, a Seyfert 1.2 with a similar 25/60 ratio (i.e., similar viewing angle) to H1834-653 and for which the AGN is viewed through an edge-on dust lane in its host galaxy (Wolstencroft et al. 1995). By contrast there are two broad-lined AGNs (3C 48 and PG 1613+658) in the E94 sample that have mid-IR colors similar to Seyfert 2 galaxies. Again the relative AGN and host galaxy luminosities cannot explain the galaxy-like IR colors in these sources, and both have optical–mid-IR luminosities in the AGN range ($\sim 10^{45}$ ergs s^{-1}) and small host galaxy contributions. 3C 48 is a steep spectrum compact radio source, one popular model for which involves their confinement by an inhomogeneous, dense medium in the host galaxy (van Breugel et al. 1984), potentially explaining the reddening of the far-IR continuum, though the clear view of the BLR remains a puzzle. For PG 1613+658 there is no obvious explanation beyond invoking an unusually strong far-IR starburst component as suggested by the detection of CO in this source (Evans et al. 2001).

Summarizing the last two sections, a simple unified model can not explain the behavior of the *HEAO* SEDs. A relation between Seyfert type and optical/UV reddening is present in the sense that bluer AGNs are mostly Seyfert 1 galaxies, and redder AGNs are mostly intermediate or type 2 Seyfert galaxies. This relation does not extend to the IR in a way consistent with standard optically thick torus models as the 25/60 ratios are similar in Seyfert galaxies with differing type and optical/UV reddening (except for non-HBLR

Seyfert galaxies). However, they can be explained by a lower optical depth, disklike structure whose obscuring column density is a function of viewing angle. If we further include the effects of differing ratios of host galaxy to AGN luminosity, most of the observed properties can be explained.

4.3. *Models*

The lower optical depths ($N_H \sim 10^{22}$–10^{23} cm^{-2}) for the obscuring material favored by our results suggest that the AGNs may be able to heat a larger amount of dust to a larger range of temperatures than in the optically thick torus models. This raises the question of whether or not a cool, starburst component is required to explain the full IR continuum of AGNs. To investigate this we use the Monte Carlo radiative equilibrium technique of Bjorkman & Wood (2001), modified to work in the parameter regime of AGNs, to compute model spectral energy distributions (SEDs). In our models we assume that an isotropic point source illuminates an axisymmetric dusty disklike structure. Incident spectra for the central engine in AGN SED models are often power laws or blackbodies (e.g., Granato & Danese 1994). Instead, in our models, we use the median SED of a normal, broad-line AGNs from Elvis et al. (1994) as the incident continuum.

The dust model is that presented by Kim, Martin, & Hendry (1994) and provides a good match to the observed extinction and scattering properties of dust in the Milky Way's interstellar medium. Our SED models suffer from the same problem as other axisymmetric models in that they predict silicate emission at 10 μm, which is not generally observed. Recent work by Nenkova, Ivezic, & Elitzur (2002) suggests that this problem may be alleviated with three-dimensional multiple cloud models and does not require different dust species or environments for Seyfert 1 and 2 models (e.g., Efstathiou & Rowan-Robinson 1995). There have been many theoretical studies of the shapes of SEDs from different axisymmetric dusty tori (e.g., Pier & Krolik 1993; Efstathiou & Rowan-Robinson 1995; Granato & Danese 1994) and more recently three-dimensional multiple dust cloud models (Nenkova et al. 2002). Our SED modeling, while using a different technique for the numerical radiation transfer, adopts an axisymmetric structure (hereafter called dusty disk) for the torus as in the papers cited above. We adopt the following density structure:

$$\rho = \rho_0 (R_0/\varpi)^{\alpha} \exp -\tfrac{1}{2}[z/h(\varpi)]^2 . \quad (1)$$

In this equation we work in units of $R_0 = 1$ pc, ρ_0 is the dusty disk density at R_0, ϖ is the radial coordinate in the disk midplane and the scale height increases with radius, $h = h_0(\varpi/R_0)^{\beta}$. We adopt $\alpha = 0$ (radial density independent of distance) and a slightly flaring scale height with $\beta = 1.1$ and fix the radial extent of the disk at $R_{max} = 300$ pc. The parameters that we varied to fit the three SEDs are the incident luminosity L_{AGN}, scale height h_0, and total mass of the dusty disk M_{torus}. The other parameter in our modeling is the disk inclination i.

We have modeled three AGNs that span the range of SED types observed in our sample. PG 0804+761 is a typical SED, MR 2251−178 shows a rather flat SED, and IR 13218+0552 is very red. Our model fits to these three AGNs are shown in Figure 12. Our goal in this modeling is to reproduce the overall shape of the different SEDs varying as few parameters as possible. Our results are certainly not
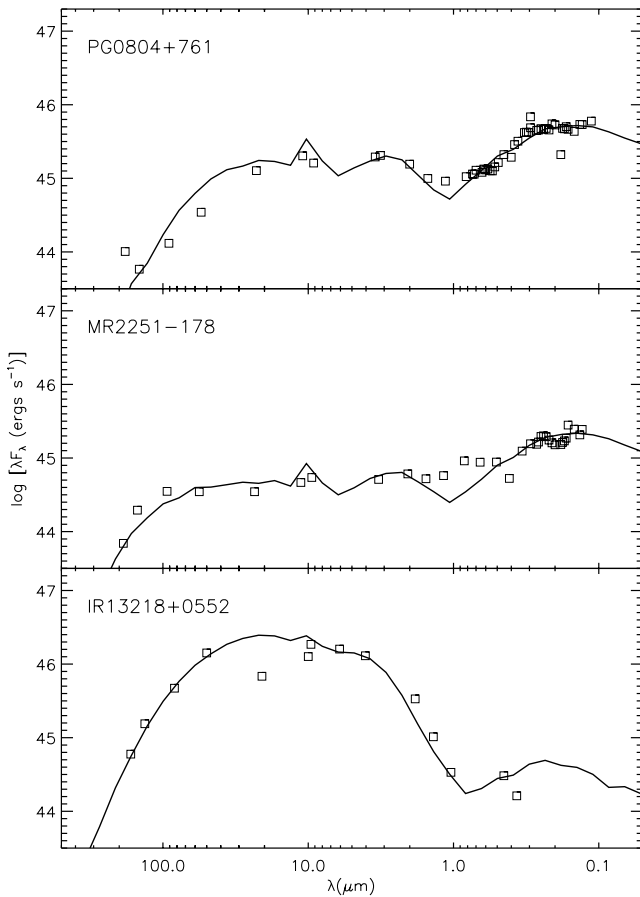
Fig. 12.—Observed SEDs for PG 0804+761, MR 2251−178, and IR 13218+0552 compared with the model SED as described in the text (§ 4.3) and Table 8.

Fig. 13.—Observed SEDs for PG 0804+761, MR 2251−178, and IR 13218+0552 superposed on their best-fit model as viewed at a range of 10 inclinations evenly spaced in cos i (starting from cos i = 0.05–0.95).

unique (e.g., see Granato & Danese 1994 for the effects of changing model parameters), but they do allow us to estimate dusty disk parameters for the three AGNs: the dusty disk mass and shape ($M_{\rm torus}$, h_0) is obtained from the level of the mid and far-IR emission. The change in SED as a function of inclination angle for the best-fit model for each AGN is shown in Figure 13. For PG 0804+761 and MR 2251−178 pole-on views satisfactorily fit the SED, while for IR 13218+0552, we require a sight line that obscures the central engine at optical wavelengths. In all cases the model SED can reproduce the full AGN SED with no requirement for an additional starburst component. The resulting model parameters are given in Table 8. The temperature and density distribution of dust in the obscuring disklike structure are shown in Figure 14. As is immediately evident the hottest dust lies at the surface and inner edge of the disk while the coolest dust with highest density is located in the plane of the disk.
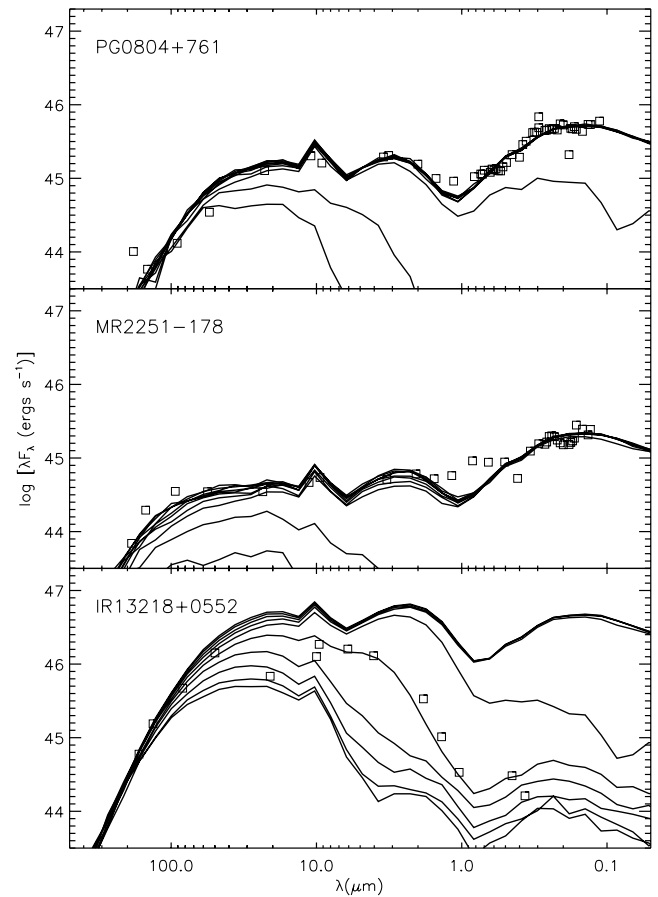
5. SUMMARY

We have studied the IR–X-ray properties of 21 *HEAO 1* A2 AGNs. The sample is hard X-ray–selected and hence relatively unbiased by the effects of obscuration. New *ISO* observations were compiled with literature data to obtain the most comprehensive radio to hard X-ray SEDs for comparison with the SEDs of radio, optically, and soft X-ray–selected samples. We found that the *HEAO* AGNs include objects with redder optical/UV continua than the optically and soft X-ray–selected AGNs, with a $B-K$ color distribution similar to radio and near-IR (2MASS) selected AGNs, although the peak of the distribution in the radio-selected samples is shifted to bluer objects. We hence estimate that ∼30%–40% of the redder AGNs may be missed by the optical and radio surveys. The bluer objects in the *HEAO* sample are mostly Seyfert 1 objects, while the redder are mostly intermediate and type 2 Seyfert galaxies, indicating that

TABLE 8
Parameters for Model SEDs That Reproduce the Observed AGN SEDs

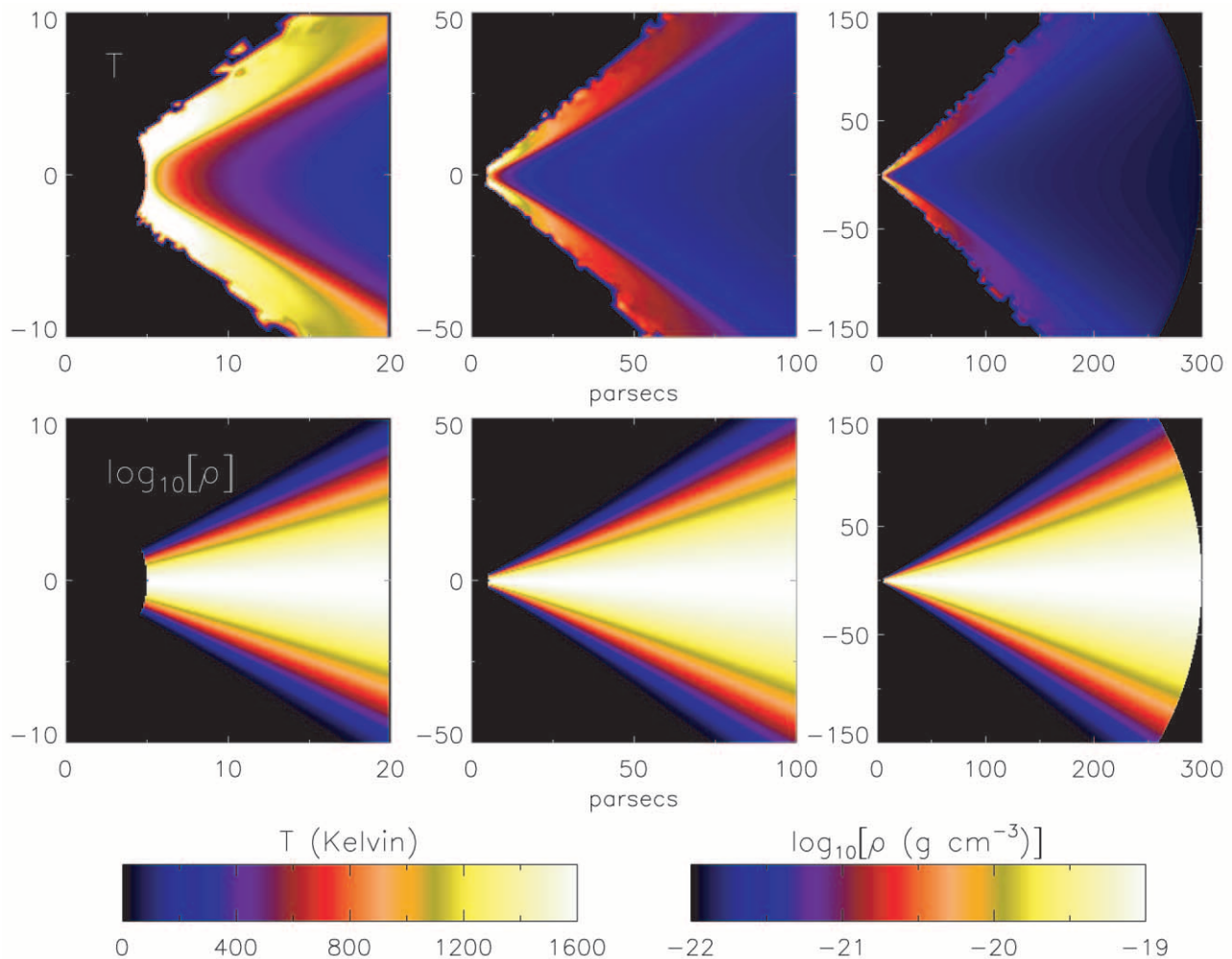| QSO Name	$L_{\rm AGN}$ ($L_\odot$)	$R_{\rm min}$ (pc)	$M_{\rm torus}$ ($M_\odot$)	h_0 (pc)	Inclination (deg)
PG 0804+761.................	6.0×10^{12}	5	3×10^8	0.04	0
MR 2251−178	2.5×10^{12}	2	8×10^9	0.025	0
IR 13218+0552..............	5.0×10^{13}	2	5×10^9	0.1	65

FIG. 14.—Temperature (*top row*) and density (*bottom row*) distributions of dust in the circumnuclear dusty disklike structure. For details see § 4.3.

Seyfert 1 galaxies have less obscured nuclei than the Seyfert 2 galaxies. This trend does not extend, however, into the IR, where the 25/60 μm flux ratios do not differ much between Seyfert types and are consistent with the ratios found in the unobscured optically selected QSO and soft X-ray–selected AGNs. There is also no correlation between the 25/60 μm flux ratio and the dust indicator from the optical/UV SEDs, indicating column densities of the order of $N_H \sim 10^{22}$ cm^{-2}, much lower than predicted by the standard compact ($\sim$few parsecs) torus model. Such a behavior can be explained if the obscuring dusty disklike structure has a lower optical depth and extends toward larger radii ($\sim$few hundred parsecs) than the standard torus, with a possibly clumpy dust distribution. We show that such a model fully explains the large range of IR SED observed in our *HEAO* sample, and since dust can be heated at larger distances, there is no need to introduce an additional starburst component to account for the far-IR emission. The range of dust temperatures is high ranging from 20 to 1000 K and the far-IR turnover occurs at wavelengths longer than 200 μm in all but three objects.

REFERENCES

Alexander, D. 2001, MNRAS, 320, L15
Andreani, P., Franceschini, A., & Granato, G. 1999, MNRAS, 306, 161
Antonucci, R. 1993, ARA&A, 31, 473
Barger, A. J., Cowie, L. L., Mushotzky, R. F., & Richards, E. A. 2001, AJ, 121, 662
Barvainis, R. 1987, ApJ, 320, 537
Beuermann, K., Thomas, H.-C., Reinsch, K., Schwope, A. D., Trümper, J., & Voges, W. 1999, A&A, 347, 47
Bjorkman, J. E., & Wood, K. 2001, ApJ, 554, 615
Boldt, E. 1987, in IAU Symp. 124, Observational Cosmology, ed. A. Hewitt, G. R. Burbidge, & L.-C. Fang (Dordrecht: Reidel), 611
Bollea, D., & Cavaliere, A. 1976, A&A, 49, 313
Boller, T., Brandt, W. N., & Fink, H. 1996, A&A, 305, 53

Brandt, N. 2001, AJ, 122, 2810
Ceballos, M. T., & Barcons, X. 1996, MNRAS, 282, 493
Chini, R., Biermann, P. L., Kreysa, E., Kuhr, H., Mezger, P. G., Schmidt, J., Witzel, A., & Zensus, J. A. 1987, A&A, 181, 237
Chini, R., Kreysa, E., & Biermann, P. L. 1989, A&A, 219, 87
Coleman, G. D., Wu, C. C., & Weedman, D. W. 1980, ApJS, 43, 393
Comastri, A., Setti, G., Zamorani, G., Elvis, M. Wilkes, B. J., McDowell, J. C., & Giommi, P. 1992, ApJ, 384, 62
Courvoisier, T. J.-L. 1998, A&A Rev., 9, 1
Cutri, R. M., Wisniewski, W. Z., Rieke, G. H., & Lebofsky, M. J 1985, ApJ, 296, 423
de Grijp, M. H. K., Miley, G. K., Lub, J., & de Jong, T. 1985, Nature, 314, 240
de Kool, M., & Begelman, M. C. 1989, Nature, 338, 484

Diplas, A., & Savage, B. D. 1994, ApJ, 427, 274
Edelson, R. A., & Malkan, M. A. 1987, ApJ, 323, 516
Efstathiou, A., & Rowan-Robinson, M. 1995, MNRAS, 273, 649
Elias, J. H., Frogel, J. A., Matthews, K., & Neugebauer, G. 1982, AJ, 87, 1029
Elvis, M., et al. 1994, ApJS, 95, 1 (E94)
Evans, A. S., Frayer, D. T., Surace, J. A., & Sanders, D. B. 2001, AJ, 121, 1893
Fadda, D., Giuricin, G., Granato, G. L., & Vecchies, D. 1998, ApJ, 496, 117
Feigelson, E. D., & Nelson P. I. 1985, ApJ, 293, 192
Fiore, F., La Franca, F., Giommi, P., Elvis, M., Matt, G., Comastri, A., Molendi, S., & Gioia, I. 1999, MNRAS, 306, L55
Gabriel, C., Acosta-Pulido, J., & Heinrichsen, I. 1998, in ASP Conf. Ser. 145, Astronomical Data and Software Systems VII, ed. R. Albrecht, R. N. Hook, & H. A. Bushouse (San Francisco: ASP), 165
Gear, W. K., et al. 1994, MNRAS, 267, 167
Giacconi, R., et al. 1979, ApJ, 230, 540
Gondhalekar, P. M., Kellett, B. J., Pounds, K. A., Matthews, L., & Quenby, J. J. 1994, MNRAS, 268, 973
Granato, G. L., & Danese, L. 1994, MNRAS, 268, 235
Granato, G. L., Danese, L., & Francheschini, A. 1997, ApJ, 486, 147
Grossan, B. A. 1992, Ph.D. thesis, MIT
Haas, M., Chini, R., Meisenheimer, K., Stickel, M., Lemke, D., Klaas, U., & Kreysa, E. 1998, ApJ, 503, L109
Haas, M., Müller, S. A. H., Chini, R., Meisenheimer, K., Klaas, U., Lemke, D., Kreysa, E., & Camenzind, M. 2000, A&A, 354, 453
Hasinger, G., et al. 2001, A&A, 365, L45
Heisler, C. A., & De Robertis, M. M. 1999, AJ, 118, 2038
Heisler, C. A., Lumsden, S. L., & Bailey, J. A. 1997, Nature, 385 700
Hildebrand, R. H. 1983, QJRAS, 24, 267
Hooper, E. J., Wilkes, B. J., McLeod, K. K., Elvis, M. S., Impey, C. D., Lonsdale, C. J., Malkan, M. A., & McDowell, J. C. 1999, in The Universe as Seen by ISO, ed. P. Cox, & M. Kessler (SP-427; Noordwijk: ESA), 893
Hornschemeier, A. E., et al. 2001, ApJ, 554, 742
Hughes, D. H., Robson, E. I., Dunlop, J. S., & Gear, W. K. 1993, MNRAS, 263, 607
Hutchings, J. B., Crampton, D., & Campbell, B. 1984, ApJ, 280, 41
Hutchings, J. B., & Gower, A. C. 1985, AJ, 90, 405
Hutchings, J. B., Janson, T., & Neff, S. G. 1989, ApJ, 342, 660
Hyland, A. R., & Allen, D. A. 1982, MNRAS, 199, 943
Impey, C. D., & Neugebauer, G. 1988, AJ, 95, 307
Isobe, T., Feigelson, E. D., & Nelson P. I. 1986, ApJ, 306, 490
Jaffe, W., Ford, H. C., Ferrarese, L., van den Bosch, F., & O'Connell, R. W., Nature, 364, 213
Jahoda, K., & Mushotzky, R. F. 1989, ApJ, 346, 638
Kellerman, K. I., Sramek, R., Schmidt, M., Shaffer, D. B., & Green, R. 1989, AJ, 98, 1195
Kim, S.-H., Martin, P.G., & Hendry, P. D. 1994, ApJ, 422, 164
Kotilainen, J. K., Ward, M. J., Boisson, C., DePoy, D. L., & Smith, M. G. 1992, MNRAS, 256, 125
Laor, A., & Drain, B. T. 1993, ApJ, 402, 441
Lemke, D., et al. 1996, A&A, 315, L64
Low, F. J., Cutri, R. M., Kleinmann, S. G., & Huchra, J. P. 1989, ApJ, 340, L1
Lumsden, S. L., Heisler, C. A., Bailey, J. A., Hough, J. H., & Young, S. 2001, MNRAS, 327, 459
MacKenty, J. W. 1990, ApJS, 72, 231
Maiolino, R., Marconi, A., Salvati, M., Risaliti, G., Severgnini, P., Oliva, E., La Franca, F., & Vanzi, L. 2001, A&A, 365, 28
Malizia, A., Bassani, L., Zhang, S. N., Dean, A. J., Paciesas, W. S., & Palumbo, G. G. C. 1999, ApJ, 519, 637
Marshall, F. E., Boldt, E. A., Holt, S. S., Mushotzky, R. F., Rothschild, R. E., Serlemitsos, P. J., & Pravdo, S. H. 1979, ApJS, 40, 657
Masci, F. J., Drinkwater, M. J., & Webster, R. L. 1999, ApJ, 510, 703
Matveyenko, L. I., & Witzel, A. I. 1999, Astron. Lett., 25, 555
McAlary, C. W., McLaren, R. A., McGonegal, R. J., & Maza, J. 1983, ApJS, 52, 341
McLeod, K. K., & Rieke, M. J. 1994, ApJ, 420, 58
———. 1995, ApJ, 441, 96

Nenkova, M., Ivezic, Z., & Elitzur, M. 2002, ApJ, 570, L9
Neugebauer, G., Green, R. F., Matthews, K., Schmidt, M., Soifer, B. T., & Bennett, J. 1987, ApJS, 63, 615
O'Dea, C. P. 1998, PASP, 110, 493
Perola, G. C., et al. 1999, A&A, 351, 937
Piccinotti, G., Mushotzky, R. F., Boldt, E. A., Holt, S. S., Marshall, F. E., Serlemitsos, P. J., & Shafer, R. A. 1982, ApJ, 253, 485
Pier, E. A., & Krolik, J. H. 1992, ApJ, 399, L23
———. 1993, ApJ, 418, 673
Polletta, M., Courvoisier, T. J.-L., Hooper, E. J., & Wilkes, B. J. 2000, A&A, 362, 75
Rees, M. J., Silk, J. I., Werner, M. W., & Wickramasinghe, N. C. 1969, Nature, 223, 788
———. 1984, ARA&A, 22, 471
Remillard, R. A., Bradt, H. V. D., Brissenden, R. J. V., Buckley, D. A. H., Roberts, W., Schwartz, D. A., Stroozas, B. A., & Tuohy, I. R. 1993, AJ, 105, 2079
Reynolds, C. S. 1997, MNRAS, 286, 513
Rieke, G. H. 1978, ApJ, 226, 550
Risaliti, G., Gilli, R., Maiolino, R., & Salvati, M. 2000, A&A, 357, 13
Roche, P. F., Aitken, D. K., Smith, C. H., & Ward, M. J. 1991, MNRAS, 248, 606
Rowan-Robinson, M. 1995, MNRAS, 272, 737
———. 1989, MNRAS, 238, 523
Rush, B., Malkan, M. A., Fink, H. H., & Voges, W. 1996, ApJ, 471, 190
Sanders, D. B., Phinney, E. S., Neugebauer, G., Soifer, B. T., & Matthews, K. 1989, ApJ, 347, 29
Schlickeiser, R., Biermann, P. L., & Crusius-Wätzel, A. 1991, A&A, 247, 283
Schlickeiser, R., & Crusius, A. 1989, IEEE Trans Plas. Sci., 17, 245
Schwope, A., et al. 2000, AN, 321, 1
Soifer, B. T., Neugebauer, G., & Houck, J. R. 1987, ARA&A, 25, 187
Stocke, J. T., Morris, S. L., Gioia, I. M., Maccacaro, T., Schild, R., Wolter, A., Fleming, T. A., & Henry, J. P. 1991, ApJS, 76, 813
Thomas, H. C., Beuermann, K., Reinsch, K., Schwope, A. D., Truemper, J., & Voges, W. 1998, A&A, 335, 467
Tokarz, S. P., & Roll, J. 1997, in ASP Conf. Ser. 125, Astronomical Data and Software Systems VI, ed. G. Hunt & H. E. Payne (San Francisco: ASP), 140
Tozzi, P., et al. 2001, ApJ, 562, 42
Tran, H. D. 2003, ApJ, 583, 632
Turner, T. J., & Pounds, K. A. 1989, MNRAS, 240, 833
van Breugel, W. J. M., Miley, G. K., & Heckman, T. A. 1984, AJ, 89, 5
Walter, R., & Fink, H. H. 1993, A&A, 274, 105
Wang, T.-G., Lu, Y.-J., & Zhou, Y.-Y. 1998, ApJ, 493, 1
Ward M., Elvis, M., Fabbiano, G., Carleton, N. P., Willner, S. P., & Lawrence, A. 1987, ApJ, 315, 74
Webster, R. L., Francis, P. J., Peterson, B. A., Drinkwater, M. J., & Masci, F. J. 1995, Nature, 375, 469
Wilkes, B. J. 1999, in ASP Conf. Ser. 162, Quasars and Cosmology, ed. G. Ferland & J. Baldwin (San Francisco: ASP), 15
———. 2001, in ASP Conf. Ser. 232, The New Era of Wide Field Astronomy, ed. R. Clowes, A. Adamson, & G. Bromage (San Francisco: ASP), 47
Wilkes, B. J., & Elvis, M. 1987, ApJ, 323, 243
Wilkes, B. J., Hooper, E. J., McLeod, K. K., Elvis, M. S., Impey, C. D., Lonsdale, C. J., Malkan, M. A., & McDowell, J. C. 1999, in The Universe as Seen by ISO, ed. P. Cox, & M. Kessler (SP-427; Noordwijk: ESA), 845
Wilkes, B. J., Schmidt, G. D., Cutri, R. M., Ghosh, H., Hines, D. C., Nelson, B., & Smith, P. S., 2002, ApJ, 564, L65
Williams, D. R., et al. 1992, ApJ, 389, 157
Wolstencroft, R. D., Done, C. J., Scarrott, S. M., & Scarrott, R. M. J. 1995, MNRAS, 276, 460
Wood, K. S., et al. 1984, ApJS, 56, 507
Young, J. S., Allen, L., Kenney, J. D. P., Lesser, A., & Rownd, B. 1996, AJ, 112, 1903
Yuan, W., Brinkmann, W., Siebert, J., & Voges, W. 1998, A&A, 330, 108
Zombeck, M. V. 1990, Handbook of Space Astronomy and Astrophysics (2d ed.; Cambridge: Cambridge Univ. Press), 198